Available online at www.sciencedirect.com

SCIENCE DIRECT®

Journal of Computational Physics 196 (2004) 539–565

JOURNAL OF COMPUTATIONAL PHYSICS

www.elsevier.com/locate/jcp

Well balanced finite volume methods for nearly hydrostatic flows

N. Botta [a,*], R. Klein [a,b,c], S. Langenberg [a,1], S. Lützenkirchen [d]

[a] *Potsdam Institute for Climate Impact Research, Telegrafenberg C4, P.O. Box 60 12 03, 14412 Potsdam, Germany*
[b] *Konrad-Zuse-Zentrum für Informationstechnik, Berlin, Germany*
[c] *Freie Universität Berlin, Mathematik und Informatik, Berlin, Germany*
[d] *Department of Public Health, Municipality of Oslo, Norway*

Received 4 April 2002; received in revised form 7 November 2003; accepted 7 November 2003

Abstract

In numerical approximations of nearly hydrostatic flows, a proper representation of the dominant hydrostatic balance is of crucial importance: unbalanced truncation errors can induce unacceptable spurious motions, e.g., in dynamical cores of models for numerical weather prediction (NWP) in particular near steep topography. In this paper we develop a new strategy for the construction of discretizations that are "well-balanced" with respect to dominant hydrostatics. The classical idea of formulating the momentum balance in terms of deviations of pressure from a balanced background distribution is realized here through local, time dependent hydrostatic reconstructions. Balanced discretizations of the pressure gradient and of the gravitation source term are achieved through a "discrete Archimedes' buoyancy principle". This strategy is applied to extend an explicit standard finite volume Godunov-type scheme for compressible flows with minimal modifications. The resulting method has the following features: (i) It inherits its conservation properties from the underlying base scheme. (ii) It is exactly balanced, even on curvilinear grids, for a large class of near-hydrostatic flows. (iii) It solves the full compressible flow equations without reference to a background state that is defined for an entire vertical column of air. (iv) It is robust with respect to details of the implementation, such as the choice of slope limiting functions, or the particularities of boundary condition discretizations.

Keywords: Conservation laws; Hydrostatic balance; Conservation form

1. Introduction

Atmospheric motions on scales relevant for numerical weather prediction and climate modeling are small perturbations of some hydrostatic state, see [3,12,21,34]. Albeit small, such perturbations are relevant

* Corresponding author. Tel.: +49-331-288-2657; fax: +49-331-288-2600.
E-mail address: botta@pik-potsdam.de (N. Botta).
[1] Supported by the Deutsche Forschungsgemeinschaft under Contract KL611/6.

0021-9991/$ - see front matter © 2003 Elsevier Inc. All rights reserved.
doi:10.1016/j.jcp.2003.11.008

and models based on the Euler equations of compressible fluid mechanics, which do not explicitly assume a hydrostatic balance, have been introduced for research and operational purposes [2,7,10,13,17,22,38,45]. For the present purposes it suffices to consider the equations for a dry atmosphere without rotation. These equations are

$$\begin{aligned} &\rho_t + \nabla \cdot (\rho \boldsymbol{v}) = 0, \\ &(\rho \boldsymbol{v})_t + \nabla \cdot (\rho \boldsymbol{v} \bigcirc \boldsymbol{v}) + \nabla p = -\rho \nabla \Phi, \\ &(\rho e + \rho \Phi)_t + \nabla \cdot ((\rho e + p + \rho \Phi)\boldsymbol{v}) = 0, \end{aligned} \tag{1}$$

together with a state equation for the pressure $p := \varphi(\rho, \rho \boldsymbol{v}, \rho e)$, a time independent gravity potential Φ and suitable initial and boundary conditions. Nearly hydrostatic motions are such that

$$(\nabla p + \rho \nabla \Phi) \cdot \boldsymbol{k} = \mathrm{O}(\epsilon) \ll |\nabla p \cdot \boldsymbol{k}| = \mathrm{O}(|\rho \nabla \Phi \cdot \boldsymbol{k}|), \tag{2}$$

where $\boldsymbol{k} := \nabla \Phi / |\nabla \Phi|$ is a unit vector aligned with the acceleration of gravity and ϵ is of the order of magnitude of $(\rho \boldsymbol{v})_t \cdot \boldsymbol{k}$. Importantly, the smallness of ϵ is due to cancellation of almost equal quantities and the "vertical" pressure gradient $\nabla p \cdot \boldsymbol{k}$ does not vanish as $\epsilon \to 0$. For nearly hydrostatic motions, standard numerical approximations for (1) are either inaccurate or unacceptably expensive. A detailed analysis will be presented in Section 2, but the reason for inaccuracy is obvious: On grids of grid spacing h, rth order approximations to ∇p, $\rho \nabla \Phi$ introduce local truncation errors (LTE) of order h^r. Depending on the grid spacing h and on the actual value of ϵ, these spurious accelerations can be orders of magnitude larger than the true vertical momentum tendency $(\rho \boldsymbol{v})_t \cdot \boldsymbol{k}$.

This problem generally occurs in the approximation of nearly balanced solutions, the balance being often between *flux divergence* and *source term*. It arises in the numerical solution of the shallow water equations with bottom topography, in steady state reactive flows, and in many other fields. Numerical methods conceived to cope with this problem are called *well balanced methods*, see [4,14,18,30]. A natural approach for constructing well-balanced methods proceeds via balanced solutions. Here we propose to use local reconstructions of balanced states within each grid cell as building blocks of discrete approximations, and to adapt these reconstructions to the local thermodynamic conditions at each time step.

For nearly hydrostatic flows such balanced states are characterized by pressure and density distributions, $p^{(0)}$, $\rho^{(0)}$, such that

$$\left(\nabla p^{(0)} + \rho^{(0)} \nabla \Phi\right) \cdot \boldsymbol{k} = 0. \tag{3}$$

If both $\nabla p \cdot \boldsymbol{k}$ and $\rho \nabla \Phi \cdot \boldsymbol{k}$ are order ϵ deviations from $\nabla p^{(0)} \cdot \boldsymbol{k}$, $\rho^{(0)} \nabla \Phi \cdot \boldsymbol{k}$ respectively, i.e.

$$\nabla\left(p - p^{(0)}\right) \cdot \boldsymbol{k} = \mathrm{O}(\epsilon) \qquad (\rho - \rho^{(0)}) \nabla \Phi \cdot \boldsymbol{k} = \mathrm{O}(\epsilon), \tag{4}$$

then $p^{(0)}$, $\rho^{(0)}$ can be used to rewrite $(1)_2$ as

$$(\rho \boldsymbol{v})_t + \nabla \cdot (\rho \boldsymbol{v} \bigcirc \boldsymbol{v}) + \nabla \delta p = -\delta \rho \nabla \Phi,$$

with $\delta p := p - p^{(0)}$, $\delta \rho := \rho - \rho^{(0)}$ and both $\nabla \delta p \cdot \boldsymbol{k}$ and $\delta \rho \nabla \Phi \cdot \boldsymbol{k}$ of order ϵ. Any rth order approximate gradient operator will then lead to well balanced LTEs of order ϵh^r.

The distributions $p^{(0)}$, $\rho^{(0)}$ are not uniquely determined by (3). Upon integration in the vertical direction, the essential degrees of freedom are a reference pressure, say at height $z = z_0$, and a vertical stratification of the potential temperature (or of some other thermodynamic variable). By determining *local* hydrostatic reconstructions within each grid cell and at each time level independently, we use these degrees of freedom to ensure that the deviations $p - p^{(0)}$ and $\rho - \rho^{(0)}$ are everywhere small as required by (4). This approach is different from strategies working with reference states defined *globally* and used for entire vertical columns of grid cells or grid points, see [7,10,23,40], and references therein.

Numerical methods for reducing the LTE associated with the discretization of ∇p have been proposed over the past three decades, see [5,33,42] and, more recently, [23,40] and references therein. In all these approaches the governing equations – hydrostatic or non-hydrostatic Boussinesq approximations and, more recently, full compressible Navier–Stokes equations – are not formulated in a Cartesian coordinate system, say (x, z) for horizontal and vertical coordinate, respectively. Instead, a coordinate transformation to curvilinear terrain following coordinates (ξ, ς) is introduced, e.g., as proposed in [11]. In this framework, approximations to differential operators like $\partial p/\partial x$ are computed by summing up products between finite difference approximations to $\partial p/\partial \xi$, $\partial p/\partial \varsigma$ (taken along the grid coordinate lines) and approximations of the metric terms $\partial \xi/\partial x$, $\partial \varsigma/\partial x$. In this context, the balancing problem consists, roughly speaking, of finding approximations to these terms that minimize the LTE associated with $\partial p/\partial x$.

Here we follow a novel approach. It relies on a conservative finite volume formulation of the governing equations with vectors described in a Cartesian frame of reference. This is canonical in finite volume methods, but does not mean that one uses also a Cartesian computational grid, see Fig. 1. Moreover, the approach employs local approximations of $p^{(0)}$, $\rho^{(0)}$ and a discrete version of Archimedes' buoyancy principle.

Consider standard finite volume approximations of the exact pressure gradient ∇p and of the exact source term $\rho \nabla \Phi$. Let P_i, R_i be approximations of p, ρ on a cell c_i of boundary ∂c_i. Then, finite volume approximations of the cell averages $\delta_{c_i}(\nabla p)$, $\delta_{c_i}(\rho \nabla \Phi)$ of ∇p, $\rho \nabla \Phi$ on c_i read

$$\delta_{c_i}(\nabla p) \approx \frac{1}{|c_i|} \oint_{\partial c_i} P_i \boldsymbol{n} \, \mathrm{d}S, \tag{5}$$

$$\delta_{c_i}(\rho \nabla \Phi) \approx \frac{1}{|c_i|} \int_{c_i} R_i \nabla \Phi \, \mathrm{d}V, \tag{6}$$

where $\boldsymbol{n}$ is the unit vector normal to ∂c_i and pointing outwards, see Fig. 1, and we have used the divergence theorem to replace integration on c_i by a boundary integral in (5).

Note that, in numerical methods, the integrals on the right hand side are usually approximated by finite sums. This fact, however, is not relevant for our discussion. Let $P_i^{(0)}$, $R_i^{(0)}$ be exact solutions of

$$\nabla P_i^{(0)} + R_i^{(0)} \nabla \Phi = 0,$$

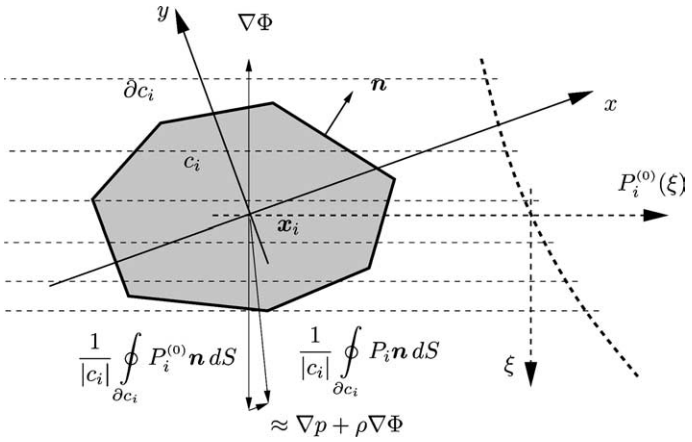

Fig. 1. Control volume c_i, acceleration of gravity $-\nabla \Phi$, local pressure $P_i^{(0)}$ and approximate $\nabla p + \rho \nabla \Phi$.

with $P_i^{(0)}$, $R_i^{(0)}$ interpolating P_i, R_i in the center x_i of c_i. Using these functions, the integral on the right hand side of (6) can be replaced, with second order accuracy, by

$$\frac{1}{|c_i|}\int_{c_i} R_i \nabla\Phi \,\mathrm{d}V = \frac{1}{|c_i|}\int_{c_i} R_i^{(0)} \nabla\Phi \,\mathrm{d}V + \mathrm{O}(h_i^2) = -\frac{1}{|c_i|}\oint_{\partial c_i} P_i^{(0)} \boldsymbol{n}\,\mathrm{d}S + \mathrm{O}(h_i^2). \tag{7}$$

We have thus approximated the source term in discrete gradient form by replacing the volume integral of $R_i^{(0)}\nabla\Phi$ by means of the boundary integral of $P_i^{(0)}\boldsymbol{n}$. This is what we referred to as discrete Archimedes' principle. The above formulation yields the following second order finite volume approximation to the average of $\nabla p + \rho\nabla\Phi$ over c_i:

$$\delta_{c_i}(\nabla p + \rho\nabla\Phi) \approx \frac{1}{|c_i|}\oint_{\partial c_i} \left(P_i - P_i^{(0)}\right)\boldsymbol{n}\,\mathrm{d}S. \tag{8}$$

A few remarks are in order here:

In the proposed formulation, numerical approximations to the gravity source term are always computed as vector quantities. As shown in (8), this is done by using the same discrete gradient operator as utilized for the computation of the approximate pressure gradient. This, together with a careful construction of $P_i^{(0)}$, allows us to control the LTEs associated with the discretization of the sum of the two terms, $\nabla p + \rho\nabla\Phi$. Having balanced these terms *as vectors* we also avoid unbalanced approximations of their horizontal components, i.e., of their components normal to $\nabla\Phi$. The present approach is currently limited to second order accuracy in space.

Our approach is independent of the number of space dimensions and does not assume any special grid arrangement. In particular, it does not rely on the alignment of one grid coordinate with the direction of the acceleration of gravity $\nabla\Phi$, and it can be used both on structured and on unstructured, e.g., triangular grids, see x, y coordinate system in Fig. 1.

It involves only local operations: $P_i^{(0)}$, $R_i^{(0)}$ are cell functions that can be computed, usually analytically, on the basis of local data. As a consequence, it can be implemented with minimal modifications of the recovery stage of standard finite volume schemes. The implementation in existing standard finite difference methods is straightforward.

By avoiding the introduction of global approximations to $p^{(0)}$, $\rho^{(0)}$, the approach proposed here does not destroy the locality of the flux function of the Euler equations. This property is essential for constructing Godunov type finite volume methods, whose built-in conservation properties make them promising candidates for climate applications. This class of schemes is considered in the present work. We plan to address a large time step semi-implicit version of the scheme in future work.

In the next section we will analyze a one-dimensional standard central scheme and explain our strategy for controlling the LTE associated with $\nabla p + \rho\nabla\Phi$ in this simple framework. We also introduce the basic notation. In Section 3 we extend these ideas and construct a class of second order well balanced Godunov type finite volume methods. In Section 4 we discuss method validation criteria and present numerical results for a second order method in one and two space dimensions.

2. Balancing in the context of central finite differences

Let $q := \{\rho, \rho\boldsymbol{v}, \rho e\}$ be an exact solution of (1) for some initial and boundary conditions, a state equation φ and a gravity potential Φ. A semi-discrete time dependent numerical method for (1) is a rule

$$\frac{\mathrm{d}Q_\omega}{\mathrm{d}t} = A_\omega(Q_\omega, \Phi)$$

to advance a set $Q_\omega(t)$ of time dependent approximations to some functionals $q_\omega(t) := \delta_\omega(q(\cdot,t))$ of $q(\cdot,t)$. These may be the values of $q(\cdot,t)$ at some set of grid points $\omega = \boldsymbol{x} := \{\boldsymbol{x}_1,\ldots,\boldsymbol{x}_n\}$

$$\delta_{\boldsymbol{x}}(q(\cdot,t)) := \{\delta_{\boldsymbol{x}_1}(q(\cdot,t)),\ldots,\delta_{\boldsymbol{x}_n}(q(\cdot,t))\} \quad \delta_{\boldsymbol{x}_i}(q(\cdot,t)) := q(\boldsymbol{x}_i,t)$$

as in finite difference methods, or the averages of q on grid cells $\omega = c := \{c_1,\ldots,c_n\}$

$$\delta_c(q(\cdot,t)) := \{\delta_{c_1}(q(\cdot,t)),\ldots,\delta_{c_n}(q(\cdot,t))\} \quad \delta_{c_i}(q(\cdot,t)) := \frac{1}{|c_i|}\int_{c_i} q(\boldsymbol{x},t)\mathrm{d}\boldsymbol{x}$$

as in finite volume methods. The rule A_ω is written in terms of consistent approximations to the functionals of the differential operators appearing in (1). For the discussion to be developed here the dependence of q, q_ω, Q_ω, A_ω on the time t is nonessential. We therefore simplify the notation and neglect the dependency of these and other quantities on t for the rest of this section.

We have pointed out that standard approximations $G_\omega(Q_\omega)$, $S_\omega(Q_\omega,\Phi)$ to $\delta_\omega(\nabla p)$, $\delta_\omega(\rho\nabla\Phi)$ introduce local truncation errors even when applied to exact, nearly hydrostatic data $Q_\omega = q_\omega$. Furthermore, on finite grids these errors can be orders of magnitude larger than the true, order ϵ, acceleration. For example, in one space dimension and on a regular grid $x_i := ih$, $i = -\infty,\ldots,\infty$ and with exact, nearly hydrostatic data $p_{x_i} := \varphi(q(x_i))$, $\rho_{x_i} := \rho(x_i)$, the approximation

$$G_{x_i} := \frac{p_{x_{i+1}} - p_{x_{i-1}}}{2h} \qquad S_{x_i} := -\rho_{x_i}\nabla\Phi(x_i) \tag{9}$$

leads, for sufficiently smooth data $\varphi(q)$, to

$$G_{x_i} - S_{x_i} = \mathrm{O}(\epsilon) + \frac{1}{6}\frac{\mathrm{d}^3\varphi}{\mathrm{d}x^3}\bigg|_{x=x_i} h^2 + \mathrm{o}(h^2). \tag{10}$$

The $\mathrm{O}(h^2)$ term clearly comes from the approximation of $\delta_{x_i}(\mathrm{d}p/\mathrm{d}x)$. In general, the problem of constructing well balanced approximations to $\delta_\omega(\nabla p)$, $\delta_\omega(\rho\nabla\Phi)$ can therefore be stated as follows.

Problem 2.1. Given a nearly hydrostatic state q in the sense of (2), and discrete approximations Q_ω to q_ω with $Q_\omega = q_\omega + \mathrm{O}(\epsilon h^r)$ on some grid of grid parameter h, find approximations $G_\omega(Q_\omega)$, $S_\omega(Q_\omega,\Phi)$ to $\delta_\omega(\nabla p)$ and $\delta_\omega(\rho\nabla\Phi)$ such that

$$\lim_{\substack{\epsilon\to 0\\ h=\text{const}}} (G_\omega - S_\omega) = 0. \tag{11}$$

This problem is difficult to solve in general and we will consider a particular case. Here we are not interested in solving the problem of reconstructing order ϵh^r approximations to q, $\varphi(q)$ from given order ϵh^r approximations to q_ω. The solution of this problem may be trivial or quite difficult depending on the order of accuracy r, on the functionals δ_ω, and on the functional form of φ, see [15].

We assume we are given exact point values $p_{\boldsymbol{x}} = \varphi(q(\boldsymbol{x}))$ of nearly hydrostatic data q. Under this assumption consider, in one space dimension and for each point x_i of a regular grid of grid spacing h, functions $P_i^{(0)}$, $R_i^{(0)}$ defined locally near x_i through

$$P_i^{(0)}, R_i^{(0)}: \quad \frac{\mathrm{d}P_i^{(0)}}{\mathrm{d}x} = -R_i^{(0)}\frac{\mathrm{d}\Phi}{\mathrm{d}x}, \quad P_i^{(0)}\Big|_{x=x_i} = p_{x_i},$$

with $P_i^{(0)}, R_i^{(0)}$ being coupled through some given distribution $\Theta_i^{(0)}$ of, e.g., the entropy (potential temperature) $\theta(p,\rho)$,

$$\theta(P_i^{(0)}(x), R_i^{(0)}(x)) = \Theta_i^{(0)}(x).$$

Moreover, let

$$P_i(x) := P_i^{(0)}(x) + (x - x_i)\frac{\left(p_{x_{i+1}} - P_i^{(0)}(x_{i+1})\right) - \left(p_{x_{i-1}} - P_i^{(0)}(x_{i-1})\right)}{2h} \quad \forall x \in \mathbb{R}.$$

$P_i^{(0)}$ and $R_i^{(0)}$ depend on the initial condition p_{x_i} and on the functions θ and $\Theta_i^{(0)}$. $\Theta_i^{(0)}$ is an approximation to θ around x_i. The only constraint we impose on $\Theta_i^{(0)}$ is that $\Theta_i^{(0)}(x_i) = \theta(p_{x_i}, \rho_{x_i})$. This constraint and the initial condition for $P_i^{(0)}$ guarantee that $P_i^{(0)}$, $R_i^{(0)}$ interpolate p, ρ at $x = x_i$, respectively. For simple choices of the thermodynamic variable θ and its local approximation $\Theta_i^{(0)}$, $P_i^{(0)}$ and $R_i^{(0)}$ can be computed analytically at virtual zero computational cost. With $P_i^{(0)}$ and P_i one can construct, for each point x_i, the following "balanced" approximations to $\delta_{x_i}(\mathrm{d}p/\mathrm{d}x)$ and $\delta_{x_i}(\rho\,\mathrm{d}\Phi/\mathrm{d}x)$

$$G_{x_i}^{\mathrm{b}} := \frac{P_i(x_{i+1}) - P_i(x_{i-1})}{2h} \qquad S_{x_i}^{\mathrm{b}} := -\frac{1}{2h}\int_{x_{i-1}}^{x_{i+1}} R_i^{(0)}(x)\frac{\mathrm{d}\Phi}{\mathrm{d}x}(x)\mathrm{d}x. \tag{12}$$

Per construction, $2hS_{x_i}^{\mathrm{b}} = P_i^{(0)}(x_{i+1}) - P_i^{(0)}(x_{i-1})$ and $\delta_{x_i}(\rho\,\mathrm{d}\Phi/\mathrm{d}x)$ has been approximated via the discrete Archimedes' buoyancy principle sketched in Section 1. Note that $G_{x_i}^{\mathrm{b}}$ and $S_{x_i}^{\mathrm{b}}$ are second order approximations to $\mathrm{d}p/\mathrm{d}x$ and $\rho\,\mathrm{d}\Phi/\mathrm{d}x$ at $x = x_i$ in the standard sense. In particular, $G_{x_i}^{\mathrm{b}} = G_{x_i}$ (see (9), left) and the local truncation error associated with this operator does not scale with ϵ. One has

$$\begin{aligned} G_{x_i}^{\mathrm{b}} - S_{x_i}^{\mathrm{b}} &= \frac{\left(p_{x_{i+1}} - P_i^{(0)}(x_{i+1})\right) - \left(p_{x_{i-1}} - P_i^{(0)}(x_{i-1})\right)}{2h} \\ &= \mathrm{O}(\epsilon) + \sum_{k=1}^{\infty}\frac{1}{(2k+1)!}\left(\left.\frac{\mathrm{d}^{2k+1}\varphi}{\mathrm{d}x^{2k+1}}\right|_{x=x_i} - \left.\frac{\mathrm{d}^{2k+1}P^{(0)}}{\mathrm{d}x^{2k+1}}\right|_{x=x_i}\right)h^{2k}. \end{aligned} \tag{13}$$

As in (10), the error associated with the approximation of $\mathrm{d}p/\mathrm{d}x + \rho\,\mathrm{d}\Phi/\mathrm{d}x$ at $x = x_i$ depends on the grid parameter h. Here, however, we have control over this error. In fact, for all $P_i^{(0)}$, $R_i^{(0)}$ constructed with the *exact* θ-distribution, i.e., with $\Theta_i^{(0)}(x) = \theta(p(x), \rho(x))$ one has

$$\left.\frac{\mathrm{d}^{2k+1}\varphi}{\mathrm{d}x^{2k+1}}\right|_{x=x_i} - \left.\frac{\mathrm{d}^{2k+1}P^{(0)}}{\mathrm{d}x^{2k+1}}\right|_{x=x_i} = \mathrm{O}(\epsilon),$$

and the scheme is well balanced. Of course this distribution is not known exactly in general but must itself be approximated discretely. In this case one can still control the balancing error by constructing higher order accurate approximations to θ, e.g., by means of polynomial reconstructions. Eq. (13) also shows that $G_{x_i}^{\mathrm{b}}$, $S_{x_i}^{\mathrm{b}}$ are well balanced for all $p = \varphi(q)$, ρ such that $\mathrm{d}\theta/\mathrm{d}x$, $\mathrm{d}\Theta_i^{(0)}/\mathrm{d}x = \mathrm{O}(\epsilon)$. This is a realistic scenario corroborated by non-dimensionalizations of a typical Brunt–Väisälä-frequency (buoyancy-frequency) of $N \sim 10^{-2}\ \mathrm{s}^{-1}$. This order of magnitude for N is equivalent with small relative entropy variations of order $\delta\theta/\theta \sim 10^{-1}$, cf. [21,32] for a discussion. The special case of a homentropic atmosphere with $\Theta_i^{(0)}$ chosen so that $\theta(p(x), \rho(x)) = \Theta_i^{(0)}(x) \equiv \text{const}$ suggests itself as a crucial analytical test case for validating our numerical approach and, up to a certain extent, its implementation, see Section 4.

As mentioned in Section 1 we cannot, at this stage, propose a method which is well balanced for *arbitrary* nearly hydrostatic initial data. However we have characterized classes of solutions for which our approach does yield well balanced approximations and we have argued that these solutions are relevant for typical atmospheric motions. For nearly hydrostatic flows not belonging to these classes of solutions, improved balancing properties can still be achieved by increasing the accuracy of the approximation of a

single scalar variable, such as the entropy or potential temperature. In Section 3 we apply this approach to construct well balanced finite volume methods in conservation form.

3. Well balanced Godunov type finite volume methods

Finite volume Godunov type methods for (1) are rules to compute numerical approximations $Q_c(t)$ to the averages $\delta_c(q(\cdot,t))$ of $q(\cdot,t)$ on some set of grid cells c. For the purpose of constructing well balanced finite volume methods we only need to consider semi-discrete time dependent rules. In one space dimension and on a regular grid $x_i := ih$, $i = -\infty,\ldots,\infty$, these have the form:

$$\begin{aligned}-h\frac{\mathrm{d}}{\mathrm{d}t}Q_{c_i}(t) &= F(Q_i(x_i+h/2,t), Q_{i+1}(x_i+h/2,t), \Phi(x_i+h/2)) \\ &\quad - F(Q_{i-1}(x_i-h/2,t), Q_i(x_i-h/2,t), \Phi(x_i-h/2)) - S_{c_i}(Q_c,\Phi).\end{aligned} \tag{14}$$

$Q_{c_i}(t)$ is a numerical approximation to $\delta_{c_i}(q(\cdot,t))$, the average of q on $(x_i-h/2, x_i+h/2)$. F is a numerical flux consistent with the flux function of (1):

$$F(q,q,\Phi) = f(q,\Phi) \qquad f(q,\Phi) := \begin{pmatrix} \rho v \\ \rho v^2 + p \\ (\rho e + p + \rho\Phi)v \end{pmatrix},$$

$S_{c_i}(Q_c,\Phi)$ is a consistent approximation to the integral of the right hand side of (1) over c_i. Equipped with a quadrature rule for time integration and with some initial cell average, (14) yields finite volume methods in conservation form. The function $Q_i(\cdot,t)$ is an approximation to the exact solution $q(\cdot,t)$ on the ith cell c_i. Let $Q(\cdot,t)$ be the relation obtained by piecing together all local approximations $Q_i(\cdot,t)$ i.e. $\forall x \in \mathbb{R}$

$$Q(x,t) := Q_i(x,t) \quad \text{for } x \in [x_i - h/2, x_i + h/2].$$

For the rest of this section we will simplify the notation and drop the dependency of all quantities on time. Q is reconstructed from the approximate cell averages Q_c. In standard methods it is a piecewise polynomial function of degree one or two, see, e.g., [29]. On each cell, degree one approximations to q can be easily constructed by localizing the cell averages in the cell centers and adding an approximation to $\mathrm{d}q/\mathrm{d}x$ in the cell centers to the localized values. This approximation is usually computed by comparing neighboring finite differences through a limiting function $\mathscr{L}$

$$Q_i(x) := Q_{c_i} + (x - x_i)\mathscr{L}\left(\frac{Q_{c_i} - Q_{c_{i-1}}}{h}, \frac{Q_{c_{i+1}} - Q_{c_i}}{h}\right) \quad \forall x \in \mathbb{R}. \tag{15}$$

$\mathscr{L}$ is constructed for Q to satisfy two conditions. The first condition requires Q to be a second order approximation to q for smooth exact data $Q_c = \delta_c(q)$. The second condition requires the total variation of Q to be less or equal to the total variation of Q_c in order to avoid spurious oscillations in the vicinity of sharp transitions, see [29].

In the previous section we have seen how to construct well balanced approximations to the grid point values of $\mathrm{d}p/\mathrm{d}x + \rho\,\mathrm{d}\Phi/\mathrm{d}x$ from given exact grid point values of $p = \varphi(q)$ and ρ. The task proved to be particularly straight-forward for homentropic and weakly stratified data. The approach consisted of three steps: first compute hydrostatically balanced local approximations $P_i^{(0)}$, $R_i^{(0)}$ to the hydrostatic components $p^{(0)}$, $\rho^{(0)}$ of $p = \varphi(q)$ and ρ. Second, construct local approximations P_i to p by adding linear approximations of $p - p^{(0)}$ to $P_i^{(0)}$. Third, given linear functionals $G_{x_i}^{\mathrm{b}}$, construct consistent discretizations $S_{x_i}^{\mathrm{b}}$ of the source term which exactly balance the local hydrostatic components $G_{x_i}^{\mathrm{b}}(P_i^{(0)})$. The keys for constructing $S_{x_i}^{\mathrm{b}}$ were the hydrostatic relationship between $P^{(0)}$ and $R^{(0)}$ imposed in step 1 per construction *and* the linearity of $G_{x_i}^{\mathrm{b}}$.

These steps can be extended to Godunov type finite volume methods by replacing standard piecewise polynomial reconstructions with functions involving the local approximations $P_i^{(0)}$, $R_i^{(0)}$ in analogy with the derivations in Section 2. There is a caveat, however. In Godunov type methods the discrete pressure gradient is not a stand alone quantity. It is a component of the discrete flux divergence appearing on the right hand side of (14). The flux divergence depends, through the numerical flux function, both on the interface values of Q_i *and* of Q_{i-1} and Q_{i+1}. We can still apply the 3-tier approach of Section 2 but we must be able to ensure that, in the limit of exactly hydrostatic data, Q is continuous through cell interfaces. If this condition is not satisfied the approximate flux divergence will depend both on Q_i and, through the numerical flux function, on Q_{i-1} and Q_{i+1} in a non-trivial and non-linear fashion. In this case it is of course still possible to apply the discrete Archimedes' principle to construct a consistent discretization of the source term in gradient form. This discretization, however, will not, in general, balance the flux divergence.

On the other hand, continuity of Q *and* consistency of the numerical flux function allow for the pressure gradient component of the discrete flux divergence to be expressed explicitly: Let $x_{i\pm} := x_i \pm h/2$, and let $F_{\rho v}$, $f_{\rho v}$ denote the ρv components of the approximate and exact flux functions F and f, respectively. Then the continuity conditions

$$Q_{i-1}(x_{i-}) = Q_i(x_{i-}), \qquad Q_i(x_{i+}) = Q_{i+1}(x_{i+})$$

imply

$$\begin{aligned}
\Delta F_{\rho v,i} &:= F_{\rho v}(Q_i(x_{i+}), Q_{i+1}(x_{i+}), \Phi(x_{i+})) - F_{\rho v}(Q_{i-1}(x_{i-}), Q_i(x_{i-}), \Phi(x_{i-})) \\
&= F_{\rho v}(Q_i(x_{i+}), Q_i(x_{i+}), \Phi(x_{i+})) - F_{\rho v}(Q_i(x_{i-}), Q_i(x_{i-}), \Phi(x_{i-})) \\
&= f_{\rho v}(Q_i(x_{i+}), \Phi(x_{i+})) - f_{\rho v}(Q_i(x_{i-}), \Phi(x_{i-})) \\
&= \varphi(Q_i(x_{i+})) - \varphi(Q_i(x_{i-})) + \rho v^2(Q_i(x_{i+})) - \rho v^2(Q_i(x_{i-})).
\end{aligned} \tag{16}$$

This information is crucial for the subsequent construction of a consistent well balanced discretization in that we will require cell interface discontinuities of the reconstructed distributions, such as $Q_i(x_{i-}) - Q_{i-1}(x_{i-})$, to vanish sufficiently rapidly as $\epsilon \to 0$.

Let $\mathscr{T}$ be the transformation which maps q to the so-called primitive variables u: density, velocity and pressure:

$$\mathscr{T}: \quad \mathbb{R}^N \ni q := \begin{pmatrix} \rho \\ \rho \boldsymbol{v} \\ \rho e \end{pmatrix} \to u = \mathscr{T}(q) := \begin{pmatrix} \rho \\ \rho \boldsymbol{v}/\rho \\ \varphi(q) \end{pmatrix} \in \mathbb{R}^N.$$

N is equal to 2 plus the number of space dimensions. For the one-dimensional finite volume method described above $N = 3$. We describe the construction of a well balanced finite volume method in this case. The extension to the multidimensional case and to the case in which the equations are augmented by some evolution equation for tracers, water vapor, or chemical species is straightforward, see Algorithms 1 and 2 in Section 4. Let $U_{c_i} = \{R_{c_i}, V_{c_i}, P_{c_i}\} = \mathscr{T}(Q_{c_i})$ denote the primitive variables associated with the approximate cell averages. As with Q_{c_i} we localize these values in the cell centers $\boldsymbol{x}_i$. This is consistent with second order accuracy. In this manuscript we stay within the framework of second order methods and use Q_{c_i} (and U_{c_i}, R_{c_i}, etc.) to denote both approximate cell averages and approximate cell center values. For the much more involved problem of recovering higher order point values from higher order cell averages see [15]. On each cell, let $R_i^{(0)}$, $P_i^{(0)}$ be the functions computed in Section 2 with initial values $P_i^{(0)}|_{x=x_i} = P_{c_i}$ and with $\Theta_i^{(0)}$ satisfying the interpolation condition $\Theta_i^{(0)}(x_i) = \theta(P_{c_i}, R_{c_i})$. Then $R_i^{(0)}$, $P_i^{(0)}$ interpolate R_{c_i}, P_{c_i} in $x = x_i$, respectively. Let also $V_i^{(0)}(x) := V_{c_i}\ \forall x \in \mathbb{R}$.

With $U_i^{(0)} := \{R_i^{(0)}, V_i^{(0)}, P_i^{(0)}\}$ one can construct a local approximation $Q_i^{(0)}$ to the hydrostatic component of q in each cell:

$$Q_i^{(0)}(x) := \mathscr{T}^{-1}\left(U_i^{(0)}(x)\right) \quad \forall x \in \mathbb{R}.$$

With $Q_i^{(0)}$ one can construct, again on each cell, the following local approximation to q

$$Q_i(x) := Q_i^{(0)}(x) + (x - x_i)\mathscr{L}\left(\frac{Q_i^{(0)}(x_{i-1}) - Q_{c_{i-1}}}{h}, \frac{Q_{c_{i+1}} - Q_i^{(0)}(x_{i+1})}{h}\right) \tag{17}$$

$\forall x \in \mathbb{R}$. Note that, due to the interpolation properties imposed on $R_i^{(0)}$, $P_i^{(0)}$ and $V_i^{(0)}$, $Q_i^{(0)}(x_i) = Q_{c_i}$. Thus, the numerator of the first argument of $\mathscr{L}$ can be written as $(Q_{c_i} - Q_i^{(0)}(x_i)) - (Q_{c_{i-1}} - Q_i^{(0)}(x_{i-1}))$. Similarly, the numerator of the second arguments reads: $(Q_{c_{i+1}} - Q_i^{(0)}(x_{i+1})) - (Q_{c_i} - Q_i^{(0)}(x_i))$. These expanded forms make clear that the arguments of $\mathscr{L}$ are one sided approximations to the slope of the *deviation* $q - q^{(0)}$ at $x = x_i$. We have not increased the order of accuracy of the standard reconstruction (15); $q - q^{(0)}$ is still approximated by piecewise linear functions. However, we have provided an improved representation of $q^{(0)}$ by introducing exact solutions of the hydrostatic relationship in the construction of Q_i. The last step is to define a balanced approximation for the source term $S_{c_i}(Q_c, \Phi)$. Similarly to the previous section we take

$$S_{c_i} := -\int_{x_{i-}}^{x_{i+}} R_i^{(0)}(x)\frac{\mathrm{d}\Phi}{\mathrm{d}x}(x)\mathrm{d}x = \int_{x_{i-}}^{x_{i+}} \frac{\mathrm{d}P_i^{(0)}}{\mathrm{d}x}\,\mathrm{d}x = P_i^{(0)}(x_{i+}) - P_i^{(0)}(x_{i-}). \tag{18}$$

Let us now consider the finite volume method (14) with Q_i, S_{c_i} defined according to (17) and (18), respectively. Q_i depends on the cell averages of a local neighborhood of c_i, say $n(c_i)$. In the one-dimensional case $n(c_i)$ is simply the set $\{c_{i-1}, c_i, c_{i+1}\}$. We say that c_i is in local hydrostatic balance with its neighborhood $n(c_i)$ if $Q_{c_j} = Q_i^{(0)}(x_j)$ $\forall j : c_j \in n(c_i)$ i.e., if the localized neighboring cell averages lie on the local approximate hydrostatic manifold $Q_i^{(0)}$ of c_i (Q_{c_i} is always identical to $Q_i^{(0)}(x_i)$ per construction). In this case $Q_i \equiv Q_i^{(0)}$ because $\mathscr{L}(0,0)$ is always zero for consistency. Consider a set of cell averages Q_c in local hydrostatic balance i.e.

$$Q_c : \quad Q_{c_j} = Q_i^{(0)}(x_j) \quad \forall j : c_j \in n(c_i) \quad \forall i : c_i \in c.$$

Also, let the flow velocity be identically zero i.e. $v_{c_i} = 0$ $\forall c_i \in c$. Then, under suitable boundary conditions, we should expect Q_c to be exactly balanced and therefore a fixed point of (14). This is indeed the case, provided Q is continuous through cell interfaces. In this case (16) and (18) imply, together with $Q_i = Q_i^{(0)}$

$$\begin{aligned} -h\frac{\mathrm{d}}{\mathrm{d}t}Q_{c_i} &= \varphi(Q_i(x_{i+})) - \varphi(Q_i(x_{i-})) - \left(P_i^{(0)}(x_{i+}) - P_i^{(0)}(x_{i-})\right) \\ &= \varphi\left(Q_i^{(0)}(x_{i+})\right) - \varphi\left(Q_i^{(0)}(x_{i-})\right) - \left(P_i^{(0)}(x_{i+}) - P_i^{(0)}(x_{i-})\right) = 0. \end{aligned} \tag{19}$$

This analysis can be easily extended to the multidimensional case in which, in general, the acceleration of gravity $-\nabla\Phi$ is not aligned with any grid coordinate. In the x–z slice model shortly described in Section 4, for instance, the neighborhood $n(c_{i,j})$ of an internal cell is the set $\{c_{i-1,j}, c_{i+1,j}, c_{i,j}, c_{i,j-1}, c_{i,j+1}\}$ and a multidimensional analog of (19) can be easily derived. The continuity of Q implies some restrictions both on the classes of data for which the method can be exactly balanced and on the choice of the *entropy* functions used to construct $Q_i^{(0)}$. Homentropic data $Q_c : \theta(\varphi(Q_c), \rho_c) = \text{const.}$ are, under the assumptions discussed above and for $\Theta_i^{(0)} = \theta(\varphi(Q_{c_i}), \rho_{c_i}) = \text{const.}$, exactly balanced.

Thus, homentropic, zero velocity initial data with suitable boundary conditions are a natural starting point for validating implementations of well balanced methods: a failure to preserve such initial data unmistakably indicates some implementation error. Homentropic, zero velocity initial data characterize the first case discussed in Section 4.

4. Method validation criteria and results

In Section 3 we have proposed a strategy for constructing well balanced Godunov type finite volume methods. We have avoided specifying important components of the method – among others the time discretization, the limiting function $\mathscr{L}$, the numerical flux F and the state equation φ – and suggested that any standard method defined in terms of these components can be modified to survive the hydrostatic limit by simply replacing recovery and source term discretization.

Of course, we have, either implicitly or explicitly, required $\mathscr{L}$, F, φ and, in general, the standard method to satisfy some reasonable assumptions. Under these assumptions, e.g., consistency of the numerical flux, we have shown in Section 3 that zero velocity, hydrostatically balanced homentropic data are, for $\Theta_i^{(0)} = \theta(\varphi(Q_{c_i}), \rho_{c_i})$, stationary solutions of the modified method (14), (17) and (18). Thus, we have identified a class of discrete solutions for which the modified method is exactly balanced. Ideally we would like to show that, again under reasonable assumptions, any standard method, when modified according to our strategy,

- is well balanced in that initial data satisfying (2) generate order ϵ accelerations independently of the grid size, h,
- converges, and
- is second order accurate.

Moreover, it would be desirable to construct particular well balanced methods which yield accurate results for standard benchmark problems, as described, e.g., in [2,19,20,35,39].

In this section we give some numerical evidence that, at least for a particular method, these goals are achieved. We start with a specification of the concrete method we have implemented for simulating the flow of a calorically perfect gas. The equation of state used below reads

$$\varphi(q) = \varphi(\rho, \rho\boldsymbol{v}, \rho e) := (\gamma - 1)(\rho e - 1/2\rho\boldsymbol{v}\cdot\boldsymbol{v}),$$

with $\gamma = 1.4$. $\nabla\Phi$ is taken to be constant and equal to $g\boldsymbol{k}$ where g is the acceleration of gravity and $\boldsymbol{k}$ is one of the unit basis vectors of a Cartesian frame of reference. Two dimensional computations have been done on a curvilinear grid fitted to the bottom topography. In all computations we have used uniform spacing both in the horizontal and in the vertical direction, the latter being that oriented in the direction of $\boldsymbol{k}$. Thus, in a two dimensional domain

$$\mathbb{R}^2 \supset \Omega := \left\{x^1, x^2 : x^1 \in [a, b], x^2 \in [z_b(x^1), z_t(x^1)]\right\}$$

between some bottom topography $x^2 = z_b(x^1)$ and some upper boundary $x^2 = z_t(x^1)$, the coordinates $x^1_{i,j}$, $x^2_{i,j}$ of the i,jth grid point are computed according to the Gal-Chen and Sommerville terrain-following curvilinear coordinates [11] commonly used in NWP models:

$$x^1_{i,j} := x^1_i = a + i(b-a)/(n_1 - 1),$$
$$x^2_{i,j} := z_b(x^1_i) + j\left(z_t(x^1_i) - z_b(x^1_i)\right)/(n_2 - 1)$$

for $i \in [0, n_1 - 1]$, $j \in [0, n_2 - 1]$. The finite volumes $c_{i,j} \in c$ have been constructed by connecting the grid points by means of straight line segments. In all cell centers, we assume that a mapping $\mathscr{J}$ from a computational space $\boldsymbol{y} := \{y^1, y^2\}$ into the physical space $\boldsymbol{x} := \{x^1, x^2\}$ exists, is regular and such that:

$$y^k = (\mathscr{J}^{-1}(\boldsymbol{x}_{i,j}))^k = \begin{cases} i & \text{if } k = 1, \\ j & \text{if } k = 2. \end{cases}$$

Time integration is done with the standard 2 step Runge–Kutta method. The maximal time step $\Delta t^{\max}$ is estimated as follows

$$\Delta t^{\max} := \min_{\omega \in c} \left(\sum_{k=1}^{2} \frac{1}{\Delta t^{\max}_{\omega,k}} \right)^{-1}, \quad \Delta t^{\max}_{\omega,k} := \min\left(\Delta t^{\max}_{\omega,k-}, \Delta t^{\max}_{\omega,k+} \right).$$

$\Delta t^{\max}_{\omega,k}$ is the maximal time step which can be used for an explicit update of ω based on the fluxes through the interfaces, $\partial\omega_{k-}$ and $\partial\omega_{k+}$ crossed by the kth coordinate lines. For $\omega = c_{m,n}$, for instance, $\partial\omega_{1\pm} = c_{m,n} \cap c_{m\pm1,n}$ and $\partial\omega_{2\pm} = c_{m,n} \cap c_{m,n\pm1}$. $\Delta t^{\max}_{\omega,k-}$ and $\Delta t^{\max}_{\omega,k+}$ are computed according to the following CFL rules, [37]:

$$\Delta t^{\max}_{\omega,k\pm} := \frac{\pm|\omega|}{|\partial\omega_{k\pm}| \max\limits_{p} \left(\lambda_p(Q_{\omega_{k\pm}}, \boldsymbol{n}_{|\partial\omega_{k\pm}}), \lambda_p(Q_{\omega}, \boldsymbol{n}_{|\partial\omega_{k\pm}}), 0 \right)},$$

where $|\omega|$ is the area of ω and $|\partial\omega_{k-}|$, $|\partial\omega_{k+}|$ are the lengths of $\partial\omega_{k-}$ and $\partial\omega_{k+}$, respectively. ω_{k-} and ω_{k+} are those neighboring cells of ω which share the interfaces $\partial\omega_{k-}$ and $\partial\omega_{k+}$ with ω. $\lambda_p(q, \boldsymbol{n})$ are the eigenvalues of the Jacobian of the flux function of the Euler equations

$$f(q, \boldsymbol{n}) := \begin{pmatrix} \rho \boldsymbol{v} \cdot \boldsymbol{n} \\ \rho \boldsymbol{v}\boldsymbol{v} \cdot \boldsymbol{n} + p\boldsymbol{n} \\ (\rho e + p)\boldsymbol{v} \cdot \boldsymbol{n} \end{pmatrix}$$

of (1). $\boldsymbol{n}|_{\partial\omega_{k-}}$, $\boldsymbol{n}|_{\partial\omega_{k+}}$ are unit vectors normal to $\partial\omega_{k-}$, $\partial\omega_{k+}$, respectively, both oriented in the increasing direction of the kth coordinate. All computations have been done with $\Delta t = 0.8\Delta t^{\max}$. On each finite volume $c_{i,j} \in c$, the functions $Q^{(0)}_{i,j}$, $Q_{i,j}$ are reconstructed from the approximate cell averages Q_c and evaluated, at fixed discrete times and in the mid-points $\boldsymbol{x}_{i\pm,j}$ and $\boldsymbol{x}_{i,j\pm}$ of the interfaces between $c_{i,j}$ and $c_{i\pm1,j}$, $c_{i,j\pm1}$, respectively, according to Algorithm 1, see Fig. 2.

Algorithm 1. 2d: interface mid-point recovery

1: **for all** $i, j : i \in I_c, j \in J_c$ **do**

2: Compute $U^{(0)}_{i,j}(\xi) := \{R^{(0)}_{i,j}(\xi), \boldsymbol{V}^{(0)}_{i,j}(\xi), P^{(0)}_{i,j}(\xi)\}$ with $R^{(0)}_{i,j}(\xi)$, $P^{(0)}_{i,j}(\xi)$ such that

$$\frac{\mathrm{d}P^{(0)}_{i,j}}{\mathrm{d}\xi} = -R^{(0)}_{i,j} g, \quad P^{(0)}_{i,j}(0) = \varphi(Q_{c_{i,j}}), \quad P^{(0)}_{i,j} / R^{(0)^{\gamma}}_{i,j} = \varphi(Q_{c_{i,j}}) / R^{\gamma}_{c_{i,j}},$$

and $\boldsymbol{V}^{(0)}_{i,j} = \boldsymbol{V}_{c_{i,j}}$.

3: Compute the (vertical) distances $\xi_{i\pm1,j}$, $\xi_{i,j\pm1}$ of the neighbor cell centers $\boldsymbol{x}_{i\pm1,j}$, $\boldsymbol{x}_{i,j\pm1}$ of $c_{i,j}$ from the normal to $\boldsymbol{k}$ passing through $x_{i,j}$.

4: Evaluate $Q^{(0)}_{i,j} := \mathscr{T}^{-1}(U^{(0)}_{i,j})$ in the cell centers $\boldsymbol{x}_{i\pm1,j}$ and compute the deviation between neighboring localized approximate cell averages and the these values:
$\delta Q_{i\pm1,j} := Q_{c_{i\pm1,j}} - Q^{(0)}_{i,j}(\xi_{i\pm1,j})$, $\quad \delta Q_{i,j\pm1} := Q_{c_{i,j\pm1}} - Q^{(0)}_{i,j}(\xi_{i,j\pm1})$

5: **for** $k = 1$ to 2 **do**
6: Compute *left* and *right* approximations to the gradient of $q - q^{(0)}$ in $c_{i,j}$

$$G\delta Q^k_{i\pm,j} := \delta Q_{i\pm1,j}\frac{\partial y^1}{\partial x^k} + \frac{1}{4}\left(\delta Q_{i,j+1} - \delta Q_{i,j-1} + \delta Q_{i\pm1,j+1} - \delta Q_{i\pm1,j-1}\right)\frac{\partial y^2}{\partial x^k}$$

$$G\delta Q^k_{i,j\pm} := \frac{1}{4}\left(\delta Q_{i+1,j} - \delta Q_{i-1,j} + \delta Q_{i+1,j\pm1} - \delta Q_{i-1,j\pm1}\right)\frac{\partial y^1}{\partial x^k} + \delta Q_{i,j\pm1}\frac{\partial y^2}{\partial x^k}$$

7: Compute *limited* approximations to the gradient of $q - q^{(0)}$ in $c_{i,j}$

$$G_i\delta Q^k_{i,j} := \mathscr{L}(G\delta Q^k_{i-,j}, G\delta Q^k_{i+,j}), \qquad G_j\delta Q^k_{i,j} := \mathscr{L}(G\delta Q^k_{i,j-}, G\delta Q^k_{i,j+})$$

8: **end for**
9: Evaluate $Q_{i,j}$ at the mid-points $\boldsymbol{x}_{i\pm,j}$, $\boldsymbol{x}_{i,j\pm}$ of the interfaces between $c_{i,j}$ and its neighborhood:

$$Q_{i,j}(\boldsymbol{x}_{i\pm,j}) = Q^{(0)}_{i,j}(\boldsymbol{x}_{i\pm,j}) + (\boldsymbol{x}_{i\pm,j} - \boldsymbol{x}_{i,j})\cdot G_i\delta Q_{i,j}$$

$$Q_{i,j}(\boldsymbol{x}_{i,j\pm}) = Q^{(0)}_{i,j}(\boldsymbol{x}_{i,j\pm}) + (\boldsymbol{x}_{i,j\pm} - \boldsymbol{x}_{i,j})\cdot G_j\delta Q_{i,j}$$

10: **end for**

As mentioned in Section 2, step 2 of Algorithm 1 can be improved by means of more accurate local approximations of entropy. All computations presented in this section have been done with piecewise constant entropy profiles: $P^{(0)}_{i,j}/R^{(0)^\gamma}_{i,j} = \varphi(Q_{c_{i,j}})/R^\gamma_{c_{i,j}}$.

Note that different approximations to $\nabla(q - q^{(0)})$, $G_i\delta Q_{i,j}$ and $G_j\delta Q_{i,j}$, are used in the evaluation of $Q_{i,j}$ at cell interfaces crossed by the first and by the second coordinate lines, respectively. In the computation of these approximate gradients the metric terms $\partial y^l/\partial x^m$ have been computed by inverting the Jacobian matrix of $\mathscr{J}$. The limiting function $\mathscr{L}$ is the monotonized central limiter, see [25,41]. For scalar arguments a and b this function is

$$\mathscr{L}(a,b) := \begin{cases} 0 & \text{if } ab \leqslant 0, \\ \frac{a}{|a|}\min\left(2\min(|a|,|b|), \frac{|a+b|}{2}\right) & \text{if } ab > 0. \end{cases}$$

Whenever $\mathscr{L}$ has been applied to non-scalar arguments the above function has been applied componentwise. We have modified the numerical flux proposed by Einfeldt in [9] to account for the potential energy term as follows. Let F^{E}_ρ, $F^{\mathrm{E}}_{\rho\boldsymbol{v}}$ and $F^{\mathrm{E}}_{\rho e}$ be the components of Einfeldt's numerical flux for the Euler equations i.e. (1) with $\Phi = 0$. The numerical flux we have used for the full equations is simply $F :=$

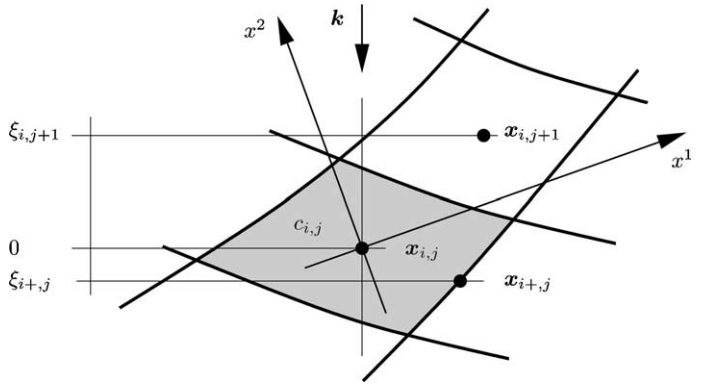

Fig. 2. Control volume $c_{i,j}$, "vertical" direction $\boldsymbol{k}$, Cartesian frame of reference (x^1, x^2), coordinate directions and distance functions.

$\{F^{\mathrm{E}}_{\rho}, F^{\mathrm{E}}_{\rho\boldsymbol{v}}, F^{\mathrm{E}}_{\rho e} + F^{\mathrm{E}}_{\rho}\Phi\}$. Since the original numerical flux is consistent with the Euler equations the modified numerical flux is consistent with (1).

Consistently with the approach outlined in Section 1 and with the analysis presented in Section 3 for the one-dimensional case, the source term has been computed with Algorithm 2.

Algorithm 2. 2d: source term computation

1: **for all** $i, j : i \in I_c, j \in J_c$ **do**
2: Compute $U^{(0)}_{i,j}(\xi) := \{R^{(0)}_{i,j}(\xi), \boldsymbol{V}^{(0)}_{i,j}(\xi), P^{(0)}_{i,j}(\xi)\}$ with $R^{(0)}_{i,j}(\xi)$, $P^{(0)}_{i,j}(\xi)$ such that
$$\frac{\mathrm{d}P^{(0)}_{i,j}}{\mathrm{d}\xi} = -R^{(0)}_{i,j} g, \quad P^{(0)}_{i,j}(0) = \varphi(Q_{c_{i,j}}), \quad P^{(0)}_{i,j}/{R^{(0)}_{i,j}}^{\gamma} = \varphi(Q_{c_{i,j}})/R^{\gamma}_{c_{i,j}},$$
and $\boldsymbol{V}^{(0)}_{i,j} = \boldsymbol{V}_{c_{i,j}}$.
3: Compute the (vertical) distances $\xi_{i\pm,j}$, $\xi_{i,j\pm}$ between the mid-points $\boldsymbol{x}_{i\pm,j}$, $\boldsymbol{x}_{i,j\pm}$ of the interfaces between $c_{i,j}$ and its neighborhood and the normal to $\boldsymbol{k}$ passing through $x_{i,j}$.
4: Evaluate $P^{(0)}_{i,j}$ at the mid-points $\boldsymbol{x}_{i\pm,j}$, $\boldsymbol{x}_{i,j\pm}$ of the interfaces between $c_{i,j}$ and its neighborhood and compute the approximate the source term
$$S_{c_{i,j}} := \frac{1}{|c_{i,j}|}\int_{c_{i,j}} R^{(0)}_{i,j}\nabla\Phi\,\mathrm{d}V = -\frac{1}{|c_{i,j}|}\oint_{\partial c_{i,j}} P^{(0)}_{i,j}\boldsymbol{n}\,\mathrm{d}S$$
with exactly the same quadrature rule which is used for computing the discrete flux divergence (from the interface mid-point values recovered as in Algorithm 1).
5: **end for**

In spite of the fact that we are actually using a grid in which one family of coordinate lines are in fact straight lines parallel to $\boldsymbol{k}$, the algorithms sketched above do not rely on this assumption and the method can be used on general curvilinear grids. Note also the correspondence between Algorithms 1 and 2. It is this correspondence (together, as shown in Section 3 for the one-dimensional case, with the continuity of the reconstruction across cell interfaces and with the consistency of the numerical flux) that guarantees that, for cell averages Q_c in local hydrostatic balance

$$Q_c: \quad Q_{c_{i,j}} = Q^{(0)}_{m,n}(x_{i,j}) \quad \forall i, j : c_{i,j} \in n(Q_{m,n}) \quad \forall m, n : c_{m,n} \in c,$$

the discrete flux divergence constructed with the mid-point values $Q_{i,j}(\boldsymbol{x}_{i\pm,j})$, $Q_{i,j}(\boldsymbol{x}_{i,j\pm})$ computed in Algorithm 1 exactly balances the source term of Algorithm 2 leading thus to exact zero tendencies.

4.1. Method implementation and stability

Here we check our implementation by considering the almost trivial test case of a hydrostatically balanced atmosphere at rest over non-vanishing topographical elevations. The numerical experiment is designed to show that the implementation does not fail to reproduce stationary solutions for zero velocity, hydrostatically balanced homentropic data. As shown in Section 3 for the one-dimensional case and explained in Section 1 and in the previous paragraphs for the multidimensional case, this is a property of the method. There is a caveat, however. When a discrete method is mapped into some implementation one cannot expect properties like the one we want to check to hold *exactly*. This issue arises because we are bound to operate with finite precision machine arithmetics. Therefore, implementations of equation (19) will generally not yield an exact balance but accelerations of the order of the round-off error. Since the first two terms on the right hand side of (19) are computed by different sequences of operations than the last two

terms of the same equation, this true even for initial data which are exactly representable in the available set of machine numbers.

At risk of stating the obvious let us stress that these tendencies have nothing to do with the local truncation errors of the discretization which, for the class of data considered, has been proven to be exactly balanced. On an infinite precision machine these errors would disappear whereas the LTEs of any discretization would not.

An interesting question which is closely related with important properties of the method – stability and dissipativity – is that of the fate of such perturbations. How will they evolve in time? The continuous problem has no dissipation mechanism and there is no background flow to transport perturbations downwind and advect undisturbed fields into the physical domain. The original discrete method has some built-in dissipation in the form of local truncation errors, and for sufficiently small time steps we expect the LTEs of the balanced scheme to also have the structure of some grid dependent dissipation. On the other hand, it is exactly the local truncation errors which we are influencing by our balancing technique.

Thus, it is interesting not only to assess the smallness of initial accelerations but to investigate the time evolution of these perturbations on time scales comparable with those of realistic simulations. Two such evolutions are represented on the right of Fig. 3 for the maximum norm of the vertical velocity. The two curves correspond to computations in double and single precision. Time is measured in days and vertical velocity in meters per second. Both computations have been done on the grid shown on the left of Fig. 3 where the units of length are kilometers. The initial cell averages are the cell center values of a homentropic atmosphere at rest. This is defined by the following functions of the vertical coordinate z:

$$p(z) = p_0^{-\frac{1}{\gamma-1}}\left(p_0 - \frac{\gamma-1}{\gamma} g\rho_0 z\right)^{\frac{\gamma}{\gamma-1}},$$

$$\rho(z) = \rho_0\left(\frac{p(z)}{p_0}\right)^{\frac{1}{\gamma}}, \quad \rho_0 = \frac{p_0}{RT_0}$$

$\forall z \in [0,8]$ km and with p_0, T_0, g and R equal to 10^5 $\mathrm{N\,m^{-2}}$, 288.15 K, 10 $\mathrm{m\,s^{-2}}$ and 287 $\mathrm{N\,m\,kg^{-1}\,K^{-1}}$, respectively. On the bottom boundary the condition $\boldsymbol{v}\cdot\boldsymbol{n} = 0$ has been imposed on the numerical flux by computing, for any given inner state $q := \{\rho, \rho\boldsymbol{v}, \rho e\}$ and any unit normal vector $\boldsymbol{n}$, the "reflected" outer state $q_o =: \{\rho, \rho\mathscr{R}(\boldsymbol{v},\boldsymbol{n}), \rho e\}$ with $\mathscr{R}(\boldsymbol{v},\boldsymbol{n}) := \boldsymbol{v} - 2(\boldsymbol{v}\cdot\boldsymbol{n})\boldsymbol{n}$. On the other boundaries the outer state is fixed to its initial value. The grid consists of 64 cells in the horizontal direction and 32 cells in the vertical direction

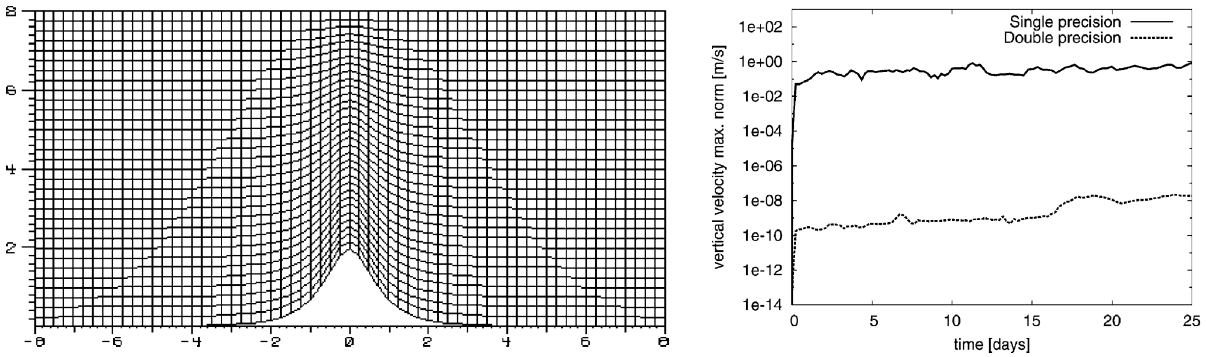

Fig. 3. Hydrostatic homentropic flow at rest above steep topography. Left: computational domain (km) and finite volumes grid (64×32). Right: vertical velocity maximum norm ($\mathrm{m\,s^{-1}}$) versus time (days).

on a 16×8 km computational domain. Thus, all cells have a width of 250 m. The vertical cell size ranges from about 190 m over the top of the mountain and 250 m on the sides of the domain.

The time step was fixed to 0.2 s throughout the computation. In the numerical results show in Fig. 3, attention is focused on the dynamics at large times. A picture of the maximal vertical velocity at short times would show that, during an initial time interval covered by about 300 steps, the tendencies are, indeed, of the order of magnitude of the round-off error, see Section 4.2. After an initial growth, the maximal vertical velocity stabilizes around values of about 1 and 10^{-8} m s^{-1} for single and double precision, respectively. Note that 10^{-8} is about twenty times the ratio between `DBL_EPSILON` and `FLT_EPSILON` (in our architecture equal to 2.2204460492503131e−16 and 1.19209290e−07F, respectively).

4.2. Smooth stratification and inversion: balancing properties

We first investigate the behavior of the well balanced scheme for smoothly stratified initial data. As in the previous case, the atmosphere is in hydrostatic balance at rest but the variable χ, which is closely related to the thermodynamic entropy or to the potential temperature, is a linear function of the vertical coordinate z:

$$\chi := \alpha^2 \frac{p}{\rho^\gamma} = \alpha^2 \frac{p_0}{\rho_0^\gamma}(1 + \sigma z), \quad \alpha := \frac{2}{\gamma - 1}.$$

This leads to the following distributions of initial pressure and density

$$p(z) = p_0^{-\frac{1}{\gamma-1}} \left(p_0 - \frac{1}{\sigma} g \rho_0 \left((1 + \sigma z)^{\frac{\gamma-1}{\gamma}} - 1 \right) \right)^{\frac{\gamma}{\gamma-1}}$$

$$\rho(z) = \rho_0 \left(\frac{p(z)}{p_0} \frac{1}{1 + \sigma z} \right)^{\frac{1}{\gamma}}, \quad \rho_0 = \frac{p_0}{R T_0}$$

$\forall z \in [0, 8]$ km. The values for p_0, T_0, g, and R are chosen as in the previous experiment. In Fig. 4 we have reported the time evolution of the maximum norm of the vertical velocity for σ equal to 1.2×10^{-6}, 1.2×10^{-5} and 1.2×10^{-4} m^{-1} and on two different grids. Time is given in minutes and vertical velocity in meters per second. The rougher grid is the same used in the previous experiment. The finer grid has twice as

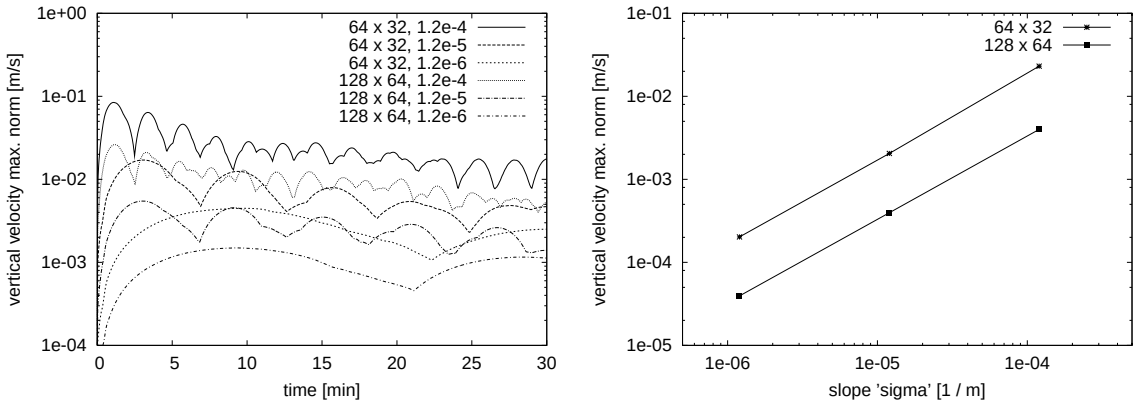

Fig. 4. Hydrostatic flow with linear χ distribution at rest above steep topography. Left: Vertical velocity maximum norm (m s^{-1}) versus time (min) for σ equal to 1.2×10^{-6}, 1.2×10^{-5} and 1.2×10^{-4} m^{-1} and 64×32 and 128×64 finite volumes grids. Right: Vertical velocity maximum norm (m s^{-1}) after 1 min versus σ (m^{-1}): 64×32 and 128×64 grids.

many cells in both directions. The case $\sigma = 1.2 \times 10^{-5}$ m^{-1} corresponds to a lapse rate of 0.0075 degrees per meter (0.0065 degrees per meter is the lapse rate of a standard atmosphere). The value $\sigma = 1.2 \times 10^{-4}$ m^{-1} corresponds to an unrealistically strongly stratified atmosphere in which the temperature increases with altitude at a rate of about 0.01 degrees per meter.

According to the analysis discussed in Section 2, the local truncation errors associated with the discretization of the difference between pressure gradient and weight vertical velocities should scale with σ times the square of the grid parameter. Thus we expect the vertical velocity to behave in much the same way. Fig. 4 shows that, at least at short times, this is indeed the case.

In order to assess the behavior of our balancing approach for more realistic stratifications, we consider the case of an atmosphere with a stable layer intersecting the topography. Geometry and discretizations are the same as in the previous experiment, see also Fig. 3. The layer is located between z_b and z_a. Inside this layer the buoyancy frequency

$$N := \sqrt{-g\left(\frac{1}{\rho}\frac{\partial\rho}{\partial z} + g\frac{\rho}{\gamma p}\right)} \tag{20}$$

is constant and equal to $N_0 + \Delta N$. Above and below this layer N is equal to N_0.

The values of z_b, z_a are 750 and 1250 m, respectively i.e. the layer is centered at a height of 1 km and is 500 m deep. The mountain top is at 2 km. We consider three cases with $N_0 = 0.01$ s^{-1} and ΔN equal to 0, 0.005 and 0.01 s^{-1} and a fourth case in which N is constant and equal to 0.02 s^{-1}. The third case corresponds to an inversion in which the temperature increases with the altitude at a rate of about 0.0014 degrees per meter. The values for p_0, T_0, g, and R are chosen as in the previous experiment. The vertical profiles of pressure, density and temperature are

$$p(z), \rho(z) = \begin{cases} p_b(z), \rho_b(z) & \text{for } z \leqslant z_b \\ p_l(z), \rho_l(z) & \text{for } z_b < z \leqslant z_a \\ p_a(z), \rho_a(z) & \text{for } z_b < z \end{cases} \qquad T(z) = \frac{p(z)}{R\rho(z)},$$

$$p_b(z) = p_0\left(1 - \frac{\gamma-1}{\gamma}\frac{1}{RT_0}\frac{g^2}{N_0^2}\left(1 - \exp\left(-\frac{N_0^2}{g}z\right)\right)\right)^{\frac{\gamma}{\gamma-1}},$$

$$p_l(z) = p_b(z_b)\left(1 - \frac{\gamma-1}{\gamma}\frac{1}{RT(z_b)}\frac{g^2}{(N_0+\Delta N)^2}\left(1 - \exp\left(-\frac{(N_0+\Delta N)^2}{g}(z-z_b)\right)\right)\right)^{\frac{\gamma}{\gamma-1}},$$

$$p_a(z) = p_l(z_a)\left(1 - \frac{\gamma-1}{\gamma}\frac{1}{RT(z_a)}\frac{g^2}{N_0^2}\left(1 - \exp\left(-\frac{N_0^2}{g}(z-z_a)\right)\right)\right)^{\frac{\gamma}{\gamma-1}},$$

$$\rho_b(z) = \rho_0\left(\frac{p_b(z)}{p_0}\right)^{\frac{1}{\gamma}}\exp\left(-\frac{N_0^2}{g}z\right),$$

$$\rho_l(z) = \rho_b(z_b)\left(\frac{p_l(z)}{p_b(z_b)}\right)^{\frac{1}{\gamma}}\exp\left(-\frac{(N_0+\Delta N)^2}{g}(z-z_b)\right),$$

$$\rho_a(z) = \rho_l(z_a)\left(\frac{p_a(z)}{p_l(z_a)}\right)^{\frac{1}{\gamma}}\exp\left(-\frac{N_0^2}{g}(z-z_a)\right).$$

Fig. 5 shows the history of the maximum norm of the vertical velocity on a 64×32 (left) and on a 128×64 (right) cell grid. For $N_0 = 0.01$ and $\Delta N = 0.005$ s^{-1}, the maximal vertical velocities are comparable with

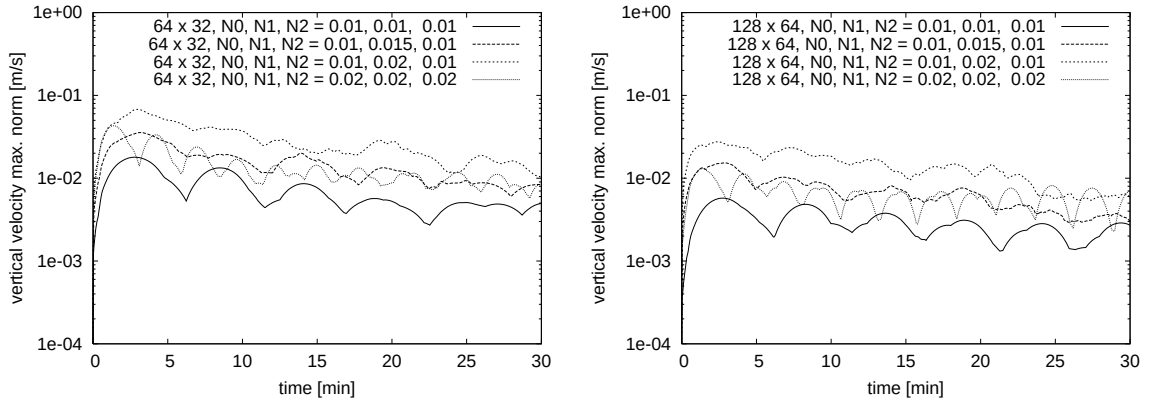

Fig. 5. Hydrostatic flow with piecewise constant buoyancy frequency N at rest above steep topography. Vertical velocity maximum norm ($\mathrm{m\,s^{-1}}$) versus time (min) for $N = N_0 + \Delta N$ for $z_b < z \leqslant z_a$ and $N = N_0$ otherwise. z_b and z_a are equal to 750 and 1250 m, respectively. Top topography at $z = 2000$ m, see Fig. 3. Four curves for $(N_0, \Delta N)$ equal to (0.01,0), (0.01,0.005), (0.01,0.01) and (0.02,0) $\mathrm{s^{-1}}$. 64×32 (left) and 128×64 cells grid.

those obtained with N constant and equal to 0.02 $\mathrm{s^{-1}}$. For the case $N_0 = 0.01$, $\Delta N = 0.01$ $\mathrm{s^{-1}}$, the maximal values of the vertical velocity are about 40% higher. In both cases, the presence of the layer across the topography does not change the order of magnitude of the vertical velocities. These are about 30 times smaller than those obtained with the standard Godunov method from which our balanced method has been derived. This is consistent with the results (not shown) that we obtained with the dynamical core of [7] which is based on well-established finite difference approximations and yields, for the same test problem and for the same model equations, maximal vertical velocities about 20 times larger than those obtained with the balanced method. The results shown in Fig. 5 can be significantly improved by replacing $\Theta_i^{(0)} = \theta(\varphi(Q_{c_i}), \rho_{c_i})$ with a more accurate approximation to θ. Preliminary results for smooth N show that local linear approximations of θ allow to reduce the vertical velocity error by about two orders of magnitude.

4.3. Accuracy and robustness

We have mentioned, in Section 1, that standard discretizations of (1) are, for nearly hydrostatic motions, either too inaccurate or too expensive. Another serious drawback is that standard approximations are not robust: numerical solutions are found to be very dependent on details of the algorithm, e.g., on the choice of the limiting function $\mathscr{L}$ and on the algorithm used to recover Q on cells near boundaries.

This sensitivity does not decrease for increasing simulation times and seriously restricts the usability of standard discretizations for, e.g., climate research. It also forces expensive and systematic investigations to assess the effects of small perturbations on the final results. Here we investigate accuracy and robustness of the well balanced method and compare them with those of a standard finite volume approximation. We consider an ideal one-dimensional atmosphere at rest between two flat plates at zero and 18,620 m. Pressure, temperature, and density are

$$p(z) = p_0 \exp\left(-\frac{T_0}{\beta}\left(1 - \sqrt{1 - \frac{2\beta g z}{R T_0^2}}\right)\right)\left(1 + \eta \exp\left(-\alpha\left(\frac{z - z_c}{H}\right)^2\right)\right),$$

$$T(z) = T_0\sqrt{1 - \frac{2\beta g z}{R T_0^2}}, \quad \rho(z) = \frac{p(z)}{R T(z)},$$

p_0, T_0, g and R are as in Section 4.1. β represents the rate of change of temperature with the logarithm of the unperturbed pressure, i.e., for η equal to zero, see [7,8]. For this case the atmosphere is in hydrostatic balance. We consider zero velocity initial data with a pressure perturbation defined by $\beta = 42$, $\eta = 10^{-3}$, $\alpha = 60$, $z_c = 9310$ m and $H = 18,620$ m. This perturbation generates weak acoustic waves which travel upwards and downwards, are reflected at the solid boundaries, and bounce back and forth between the two plates. As is known from the theory of weakly nonlinear acoustics, [16], these waves will steepen into weak shocks and begin to dissipate on time scales of order $O(H/Mc)$, equivalent to $O(1/M)$ oscillation cycles. Here c is a characteristic speed of sound and M is the characteristic Mach number for the oscillatory vertical motions. Numerical methods for non-hydrostatic models have to (1) guarantee that these waves generate spurious dynamics neither over short nor over long time scales, and to (2) avoid the CFL time step restrictions associated with the propagation of such waves. In operational methods the second requirement can be met by implicit and semi-implicit methods, sub-cycling for fast modes, or combinations of such techniques. Here we concentrate on the first issue. Consider the evolution of the initial perturbation at short times. The relative pressure perturbation

$$\frac{\varphi(q(t,\cdot)) - p|_{\eta=0}}{p|_{\eta=0}}$$

at time zero and after 12 s is shown on the left of Fig. 6. On the right of the same figure you can see the corresponding velocities (in $\mathrm{m\,s^{-1}}$). Four curves are plotted in both figures for each time. They correspond to the numerical solutions obtained with a standard method and with the well balanced method presented above. For each method 2 computations are shown: one with the monotonized central limiter and one with no limiter and central slopes, i.e., $\mathscr{L}(a,b) = (a+b)/2$. The curves are not distinguishable because all computations have been done on a very fine grid of 8192 cells. This shows that, as the grid parameter tends to zero, the numerical solutions obtained with the well balanced and standard methods converge towards the same solution.

When reconstructing a piecewise linear Q from a given set of cell averages, "left" and "right" one-sided approximations to the first derivative of the exact solution have to be evaluated in each cell. These approximations are then injected into the limiting function $\mathscr{L}$. On a one-dimensional regular grid, left and right approximations can be simply evaluated by computing first order finite differences between the local

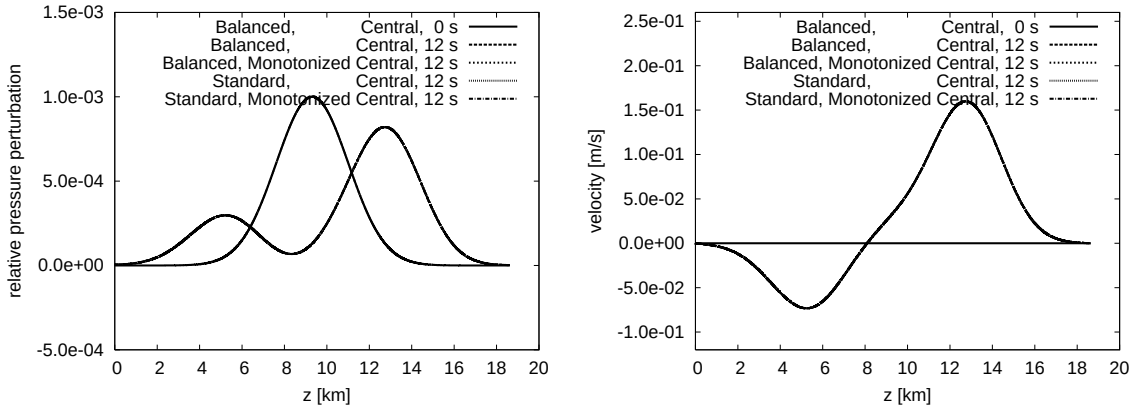

Fig. 6. Hydrostatic flow between flat plates with pressure perturbation. Relative pressure perturbation (left) and velocity (right, $\mathrm{m\,s^{-1}}$) versus altitude (km) at $t = 0$ and $t = 12$ (s). Standard and well balanced methods with monotonized central limiter and unlimited central slopes yield indistinguishable results on a high resolution grid of 8192 cells (used as reference solutions below).

cell average and the cell averages to the left and to the right. In the first and in the last cell of the grid, however, the left and the right neighbors are missing. As a consequence, the left slope in the first and the right slope in the last cell must be approximated in a different fashion. This can be done in various ways which may depend on the boundary condition imposed on the corresponding boundary. The associated procedures will be called boundary recovery algorithms below.

In the case of a rigid wall boundary condition, one can think of extrapolating the slopes from the inside by means, e.g., of the last one, two, or three inner slopes. Another strategy is to use some prescribed outer state and the values in the first (last) cell to evaluate the left (right) slope.

Figs. 7 and 8 show the reference solution of Fig. 6 and the results obtained, on coarse 32 cell grids, with a standard and with the well balanced method for different boundary recovery algorithms – among others with the algorithm used for computing the reference solution. Besides being quite inaccurate, the numerical solutions obtained with the standard method on the 32 cell grid depend sensitively on the boundary recovery algorithm. Note that, for the boundary condition considered here and in absence of a specific stability

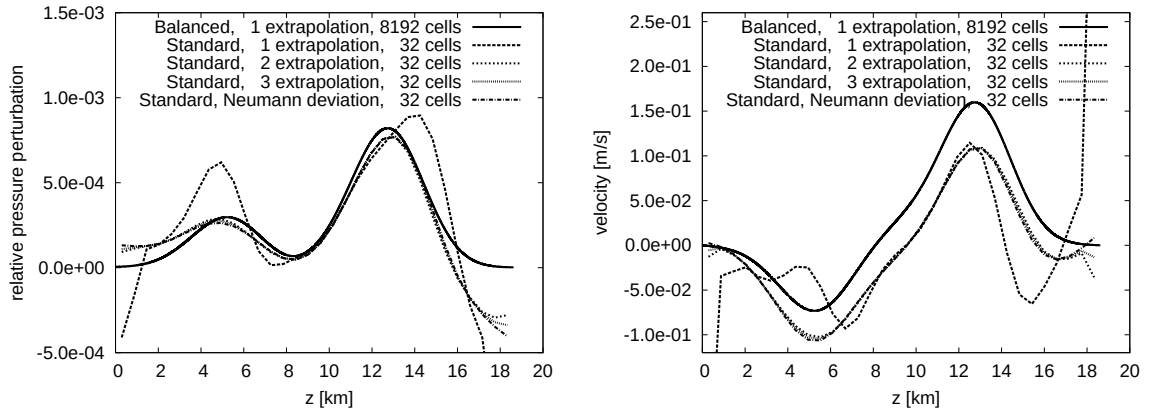

Fig. 7. Hydrostatic flow between flat plates with pressure perturbation. Relative pressure perturbation (left) and velocity (right, $\mathrm{m\,s^{-1}}$) versus altitude (km) at $t = 12$ (s). Standard method with unlimited central slopes and four different boundary recovery algorithms. Reference solution and 32 grid cells solutions.

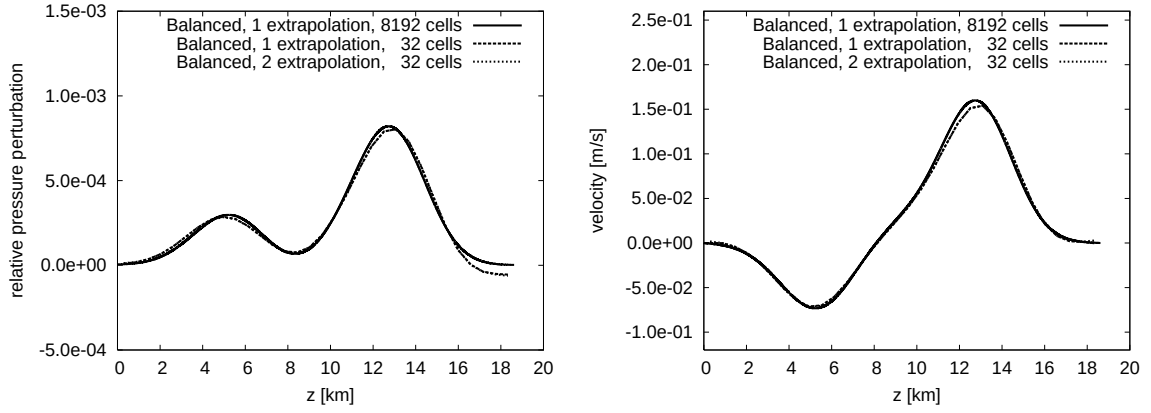

Fig. 8. Hydrostatic flow between flat plates with pressure perturbation. Relative pressure perturbation (left) and velocity (right, $\mathrm{m\,s^{-1}}$) versus altitude (km) at $t = 12$ (s). Well balanced method with unlimited central slopes and two different boundary recovery algorithms. Reference solution and 32 grid cells solutions.

analysis, there is no a priori argument for choosing a particular algorithm. A stability analysis would help restricting the set of meaningful boundary recovery algorithms but still leave a range of possible choices.

What one really would like to have is a method that does not depend in a critical way on this choice. Fig. 8 shows that the well balanced method satisfies this requirement and is far more accurate than the standard method. In fact, the standard method requires about three times more cells to achieve the same accuracy for this test case as the well balanced method.

Figs. 9 and 10 show a comparison between standard and well balanced methods for different limiting functions but with a fixed boundary recovery algorithm. We have tested unlimited central slopes, the monotonized central limiter, Van Leer's limiter and the "minmod" limiter, see [41,44]. For the standard method we have used the boundary recovery algorithm that gave the "best" results in the previous experiment. This corresponds to the dash-dot line in Fig. 7 and consists of setting to zero the slope of the deviation between the actual state and the initial condition. For the well balanced method we have simply extrapolated the approximate slope (of $q - q^{(0)}$) from the inside.

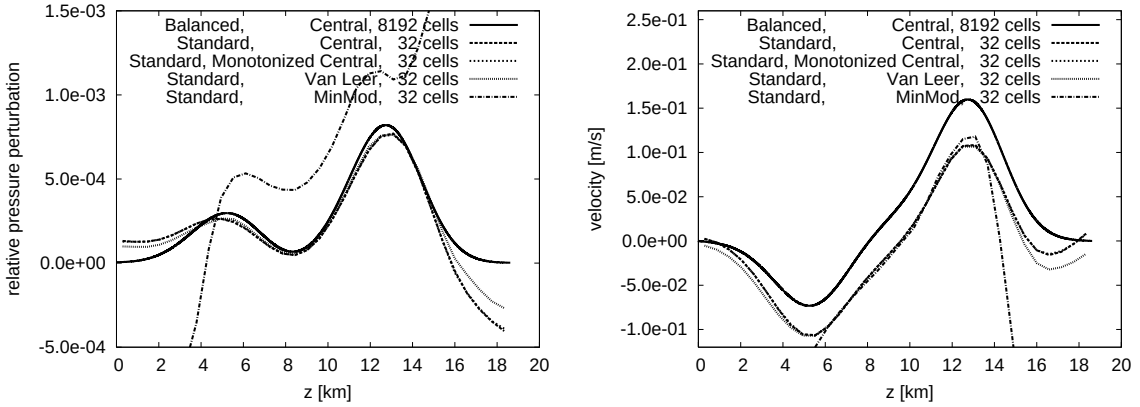

Fig. 9. Hydrostatic flow between flat plates with pressure perturbation. Relative pressure perturbation (left) and velocity (right, $\mathrm{m\,s^{-1}}$) versus altitude (km) at $t = 12$ (s). Standard method with unlimited central slopes and monotonized central, Van Leer and minmod limiters. Reference solution and 32 grid cells solutions.

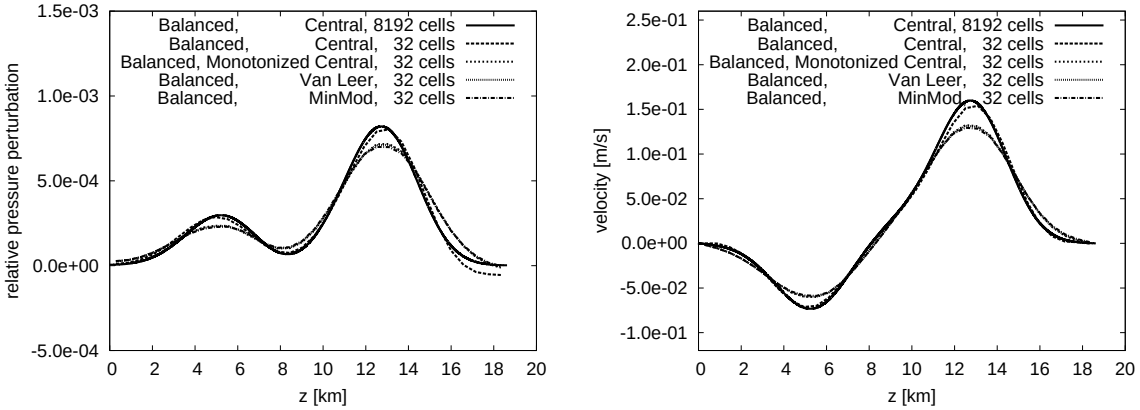

Fig. 10. Hydrostatic flow between flat plates with pressure perturbation. Relative pressure perturbation (left) and velocity (right, $\mathrm{m\,s^{-1}}$) versus altitude (km) at $t = 12$ (s). Well balanced method with unlimited central slopes and monotonized central, Van Leer and minmod limiters. Reference solution and 32 grid cells solutions.

As expected, the numerical solution obtained with the standard method depends critically on the choice of the limiting function. The same arguments used in the analysis of the sensitivity of the numerical results with respect to perturbations of the boundary recovery algorithm hold here. On very smooth functions – the ones considered here – there is no particular reason to prefer the monotonized central limiter to the Van Leer limiter and "good" numerical methods should not critically depend on this choice.

The numerical results obtained with the well balanced method have this kind of robustness. There is, of course, a significant accuracy gap between unlimited and limited computations. This is a well known problem which stems from the fact that, even on smooth solutions, the accuracy of the limited scheme in the vicinity of local extrema is not better than first order. This problem affects both the standard and the well balanced method. Note, however, that the effects of local accuracy losses on the standard method are devastating. The balancing approach proposed here can be applied to more sophisticated recovery algorithms designed to avoid local accuracy losses, see [15] and references therein.

4.4. Convergence study

In this experiment we investigate the well balanced method for the case of a flow past an idealized topography. The test case was proposed in [40] to study the impact of a new terrain-following grid on the Canadian MC2 model [1]. Two issues are discussed here: (i) The rate of convergence of the scheme, and (ii) the qualitative behavior of nearly stationary solutions on relatively coarse grids. The idealized topography is

$$z_{\mathrm{b}}(x) = h \exp\left(-\frac{x^2}{a^2}\right) \cos^2\left(\frac{\pi x}{\lambda}\right) \quad \forall x \in \mathbb{R},$$

with $h = 250$ m, $a = 5$ km and $\lambda = 4$ km. In the initial condition the buoyancy frequency (20) is constant and equal to 0.01 s^{-1}. p_0 and T_0 are equal to 10^5 $\mathrm{N\,m}^{-2}$ and 273.16 K, respectively. The vertical profiles of pressure, density and temperature are

$$p(z) = p_0\left(1 - \frac{\gamma - 1}{\gamma}\frac{1}{RT_0}\frac{g^2}{N^2}\left(1 - \exp - \frac{N^2}{g}z\right)\right)^{\frac{\gamma}{\gamma-1}},$$

$$\rho(z) = \rho_0\left(\frac{p(z)}{p_0}\right)^{\frac{1}{\gamma}} \exp - \frac{N^2}{g}z, \quad T(z) = \frac{p(z)}{R\rho(z)}$$

for z between zero and 19,500 m. The computational domain is 200 km wide. The horizontal velocity is equal to 10 $\mathrm{m\,s}^{-1}$ between zero and 10,395 m and decreases linearly to zero between 10,395 and 19,500 m. The vertical velocity is zero in the whole domain. The basic grid consists of 400×64 cells. All cells have a width of 500 m. The vertical cell size is about 300 m.

To estimate the convergence rate of the method, we consider, beside the basic grid, refinements of 800×128, 1600×256 and 3200×512 cells and compute numerical solutions after 1000, 2000, 4000 and

Table 1
Approximate 2-norm errors (deviations from finest grid solution) and convergence rates after about 8 min of simulation time

	Density	Rate	Horizontal velocity	Rate	Vertical velocity	Rate	Pressure	Rate
400×64	4.341		1.310		1.468		3.531	
800×128	1.369	1.66	0.719	0.87	0.433	1.75	0.888	1.99
1600×256	0.361	1.92	0.029	1.32	0.014	1.59	0.222	2.00
3200×512	0.0		0.0		0.0		0.0	

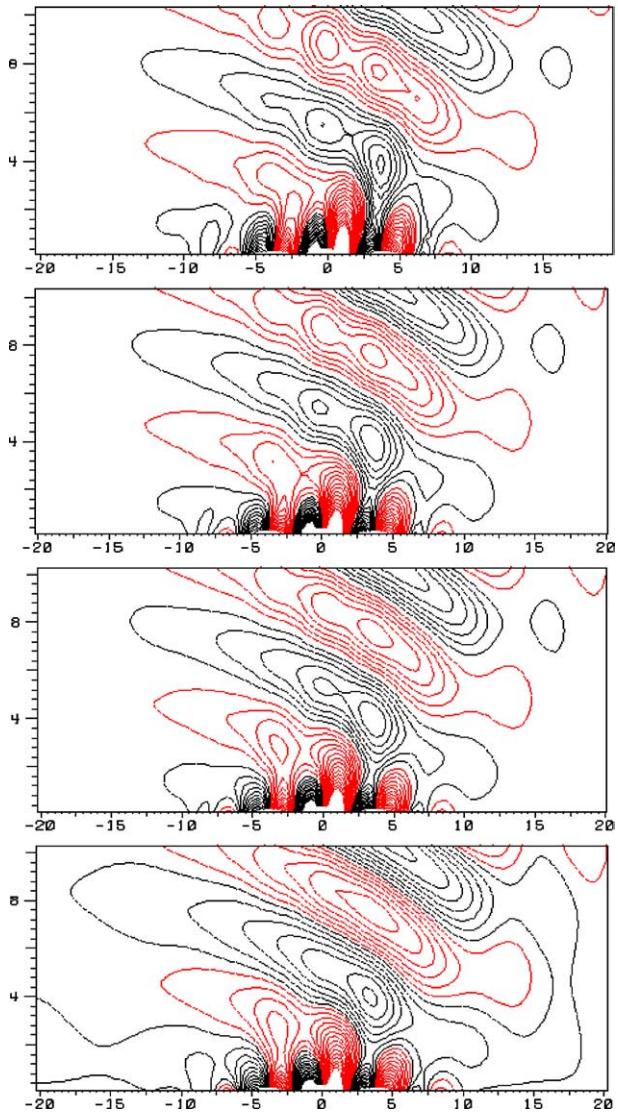

Fig. 11. Linear non-hydrostatic flow. Steady state vertical velocity near topography (40×10.8 km sub-domain). 40 contour lines between -1 and -0.05 and between 0.05 and 1 $\mathrm{m\,s^{-1}}$. Contour interval 0.05 $\mathrm{m\,s^{-1}}$. From top to bottom: 8, 10, 12 and 16 cells per half wavelength.

8000 iterations, respectively. This number of iterations corresponds to about 8 min of physical time on all grids and allows to compute the numerical solution on the finest grid with a workstation and in a reasonable time. Approximate convergence rates have been computed by comparing the numerical solutions on successive refinements of the basic grid. Errors have been estimated by taking the differences between the results obtained on the 400×64, 800×128 and 1600×256 cells grids on the one hand, and those computed on the 3200×512 cells grid on the other. Error and convergence rates are summarized in Table 1.

To study the qualitative behavior of nearly stationary solutions we consider, beside the basic grid, refinements of 500×80, 600×96 and 800×128 cells grids. In the basic grid the topography is resolved with 8

cells per half wavelength, i.e., $\lambda = 8\Delta x$. The refinements correspond to grids of 10, 12 and 16 cells per half wavelength. We compute numerical solutions after 30,000, 37,500, 45,000 and 60,000 time steps, respectively. This corresponds to about 4 hours of physical time and almost stationary solutions.

Fig. 11 shows contour lines of the vertical velocity for the four grids. On the coarsest grid (top) the topography is marginally resolved and the numerical solution has an unphysical wave pattern. This is in agreement with the results discussed in [40] for the same computational grid as used here (unsmoothed "sigma" coordinate, see [40, p. 16] and Fig. 13). As the grid is refined – from top to bottom in Fig. 11 – the unphysical pattern disappears and the numerical solution is in good agreement with the linear analytical solution.

In recent work with the Weather Research and Forecast model (WRF), see [23], it is shown that *inconsistent* approximations – approximations of different order of accuracy along different coordinate surfaces – can lead to unphysical wave patterns like those seen in Fig. 11 on rough grids. These occur here in spite of using a *consistent* scheme based on piecewise linear reconstruction and slopes computed through second order central finite differences along both coordinate lines.

It is therefore interesting to investigate the sensitivity of our results for this test problem w.r.t. perturbations of the recovery algorithm in general and of the local hydrostatically balanced state in particular. Fig. 12 shows the steady state results obtained on a grid of 10 cells per half wavelength (500×80) with our basic algorithm (left, see also Fig. 11), and with a slightly different recovery algorithm (right). In the modified recovery we have replaced the piecewise constant entropy profiles of step 2 of Algorithms 1 and 2 by means of piecewise linear approximations:

$$P_{i,j}^{(0)}/R_{i,j}^{(0)^\gamma} = \varphi(Q_{c_{i,j}})/R_{c_{i,j}}^{\gamma} + \nabla_{c_{i,j}}\Theta \cdot \left(\boldsymbol{x} - \boldsymbol{x}_{i,j}\right).$$

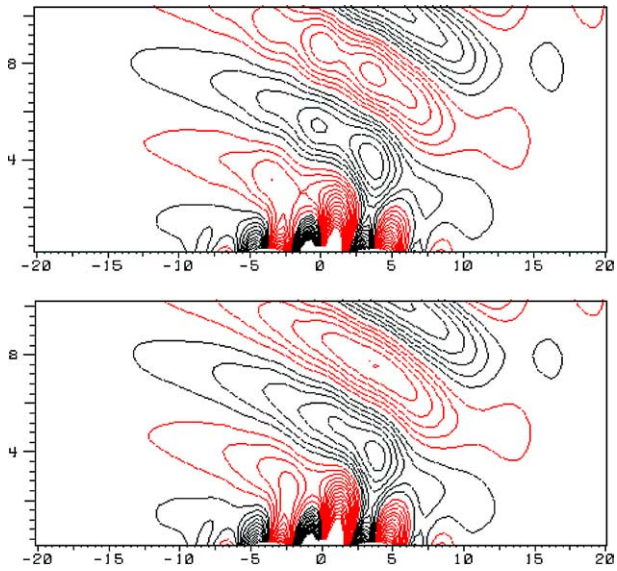

Fig. 12. Linear non-hydrostatic flow. Steady state vertical velocity near topography (40×10.8 km sub-domain). Basic scheme (top) and modified scheme with reconstruction of the local balanced state via piecewise linear entropy distribution and left and right local approximations to the gradient of $q - q^{(0)}$ as in (21) (bottom). 40 contour lines between -1 and -0.05 and between 0.05 and 1 m s^{-1}. Contour interval 0.05 m s^{-1}. 10 cells per half wavelength.

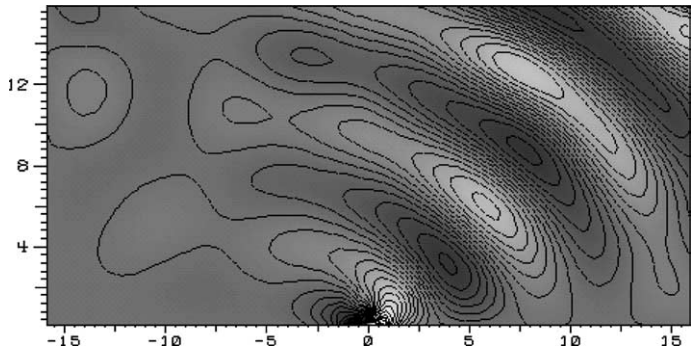

Fig. 13. Linear non-hydrostatic flow. Computational domain (km) and vertical velocity ($\mathrm{m\,s^{-1}}$) on a 128×64 cells grid.

In the above equation the discrete entropy gradient $\nabla_{c_{i,j}}\Theta$ has been computed by standard second order central finite differences along the grid lines. Moreover, we have replaced the left and right approximations to the gradient of $q - q^{(0)}$ in step 6 of Algorithm 1 with the simpler (but still *consistent* and second order accurate) approximations:

$$\begin{aligned} G\delta Q^k_{i\pm,j} &:= \delta Q_{i\pm1,j}\frac{\partial y^1}{\partial x^k} + \frac{1}{2}\left(\delta Q_{i,j+1} - \delta Q_{i,j-1}\right)\frac{\partial y^2}{\partial x^k}, \\ G\delta Q^k_{i,j\pm} &:= \frac{1}{2}\left(\delta Q_{i+1,j} - \delta Q_{i-1,j}\right)\frac{\partial y^1}{\partial x^k} + \delta Q_{i,j\pm1}\frac{\partial y^2}{\partial x^k}. \end{aligned} \tag{21}$$

With the basic scheme, the erroneous flow pattern disappears for resolutions between $\lambda = 12\Delta x$ and $\lambda = 16\Delta x$, see Fig. 11). With the modified recovery, the erroneous flow pattern disappears for resolutions somewhere between $\lambda = 8\Delta x$ (not shown here but qualitatively similar to the results obtained with the basic scheme) and $\lambda = 10\Delta x$.

4.5. Linear, non-hydrostatic gravity waves

In the previous experiment we have studied the behavior of the balanced method for a linear hydrostatic flow above a mountain-like obstacle. In this setup, the deviations of the pressure from a stationary horizontally homogeneous background state are themselves hydrostatic and the scheme, conceived to well represent nearly hydrostatic flows, performs as expected.

With the last experiment we want to test our approach for a flow in which pressure perturbations are not in hydrostatic balance. These flows are relevant for practical applications, see [2,8,19,20,39].

We consider the non-hydrostatic flow above a mountain-like obstacle. Here linear means that the Froude number based on the buoyancy frequency of the initial data and on the mountain height h, $u/(Nh)$, is much larger than one. Non-hydrostatic means, in this context, that the Froude number based on the horizontal size of the obstacle a, $u/(Na)$ is about unity. This is a standard test problem for numerical methods for weather prediction, see references above. In the limit for $u/(Nh) \to \infty$ steady state analytical solutions have been computed in [6,31,36,43].

The initial conditions consist of an isothermal atmosphere with p_0, T_0 equal to $10^5\ \mathrm{N\,m^{-2}}$ and 273.16 K, respectively. The acceleration of gravity g and the gas constants R and γ are, as in the previous examples, equal to $10\ \mathrm{m\,s^{-2}}$, $287\ \mathrm{N\,m\,kg^{-1}\,K^{-1}}$ and 1.4, respectively. In such atmosphere the buoyancy frequency N is constant and about $0.0191\ \mathrm{s^{-1}}$. This gives, with an initial horizontal velocity of $19.1\ \mathrm{m\,s^{-1}}$ and h, a equal to 100 and 1000 m, values of $u/(Nh)$ and $u/(Na)$ of 10 and 1, respectively.

As in the first and in the second experiment, the topography $z_b = h/(1 + (x/a)^2)^\alpha \ \forall x \in \mathbb{R}, \alpha = 3/2$, see [39], is a smooth function of the horizontal space coordinate x. In this test problem, the quality of the numerical results very much depends on the capability to avoid spurious reflection of the gravity waves at the lateral boundaries and at the top of the atmosphere. Here we have used boundary conditions based on the theory of characteristics at the lateral boundaries. In particular, at the top of the atmosphere, numerical fluxes have been computed using the states recovered from the inside, a constant external state, and suitably rotated Riemann problems. This approach requires further investigation and will be reported in a separate work.

The isolines of the vertical velocity on the whole computational domain are shown in Fig. 13. The results are in qualitative agreement with those reported in the literature and with the linear solution, thereby demonstrating that our well-balanced approach does not compromise non-hydrostatic effects.

5. Conclusions

Godunov-type schemes for compressible flows are widely used in computational fluid dynamics, desirable features being conservation of mass, momentum, and total energy up to machine accuracy, and robust handling of sharp discontinuities such as shocks and contact discontinuities. An extension of such a scheme by a standard (second order accurate) discretization of the gravity source term should make it applicable to atmospheric flow regimes with length scales up to several kilometers. Our investigations indicate that this is true in principle, but that unacceptably high spatial resolution is required to achieve meaningful results when the pressure gradient and gravity source term dominate the vertical momentum balance.

Unbalanced truncation errors associated with these two terms result in spurious vertical accelerations which accumulate and lead to unphysical flow patterns. Numerical methods conceived to cope with such problems are called *well balanced methods*, see [4,14,18,30]. Here we suggest a balancing strategy based on *local* approximations of hydrostatic states in each grid cell which are utilized in two ways. On the one hand, they are used in the recovery stage of a standard MUSCL [24–28] approach: Only *local deviations* from the hydrostatic states enter the usual slope limiting procedures. On the other hand, a *discrete Archimedes principle* is employed to express the gravity source term as the cell surface integral of the reconstructed hydrostatic pressure. As the pressure gradient is also represented as a surface integral in conservative finite volume methods, namely of the pressure contribution to the momentum flux, we achieve a synchronization of the truncation errors of these two dominating terms.

These modifications allow us to significantly reduce the number of grid cells needed to approximate nearly hydrostatic motions with acceptable accuracy. The approach requires the solution of a small number of scalar ordinary differential equations for each grid cell per flux evaluation. In most cases these solutions can be computed analytically so that they induce little extra computational costs.

The resulting method inherits the conservation properties of the underlying Godunov-type scheme. Several tests show that it is still capable of representing acoustic motions, it is robust against details of the implementation, e.g., the choice of slope limiting functions, it is second order accurate in space and in time, and it produces results with acceptable accuracy on relatively coarse grids for tests involving gravity wave generation over topography.

The balancing strategy proposed here, i.e., local hydrostatic reconstruction combined with a synchronization of the pressure gradient and gravity source term discretizations, should also be applicable to numerical methods other than Godunov-type finite volume schemes.

Acknowledgements

The authors thank the reviewers and the editor, whose comments have triggered various nontrivial improvements of the paper. This research was funded partly by the Deutsche Forschungsgemeinschaft,

grant DFG KL 611/6-3. This work heavily relies on free software, among others on the CGG compiler, Emacs, LaTeX, gnuplot, MeshTV, on the Debian/GNU Linux operating system and on the `util` library of D. Hempel and O. Friedrich. It is our pleasure to thank all developers of these excellent products.

References

[1] R. Benoit, M. Desdagné, P. Pellerin, Y. Chartier, S. Desjardins, The Canadian MC2: a semi-Lagrange, semi-implicit wide-band atmospheric model suited for fine-scale process studies and simulation, Month. Wea. Rev. 125 (1997) 2382–2415.
[2] L. Bonaventura, A semi-implicit semi-Lagrangian scheme using the height coordinate for a nonhydrostatic and fully elastic model of atmospheric flows, J. Comput. Phys. 158 (2000) 186–213.
[3] N. Botta, R. Klein, A. Almgren, Asymptotic analysis of a dry atmosphere, in: P. Neittaanmäki, T. Tiihonen, P. Tarvainen (Eds.), Proceedings of the 3rd European Conference ENUMATH 99: Numerical Mathematics and Advanced Applications, World Scientific, Singapore, 2000.
[4] P. Cargo, A.Y. Le Roux, Un schéma équilibre adapté au modèle d'atmosphère avec termes de gravité, C.R. Acad. Sci. Paris 318 (Série I) (1994) 73–76.
[5] A. Corby, Gilchrist, R.L. Newson, A general circulation model of the atmosphere suitable for long period integration, QJRMS 98 (1972) 809–832.
[6] R. Rotunno, D.J. Muraki, Revisiting Queney's Flow over Mesoscale Topography. Technical report, AMS mountain meteorology meeting, 2000.
[7] G. Doms, U. Schättler, The nonhydrostatic limited-area model lm (lokal-modell) of dwd: Part i, scientific documentation, Deutscher Wetterdienst, 1997.
[8] J. Dudhia, A nonhydrostatic version of the Penn State/NCAR mesoscale model: validation tests and simulation of an Atlantic cyclone and cold front, Month. Wea. Rev. 121 (1993) 1493–1513.
[9] B. Einfeldt, Zur Numerik der stoßauflösenden Verfahren. Dissertation, RWTH Aachen, 1988.
[10] J. Dudhia, G.A. Grell, D.R. Stauffer, A description of the fifth-generation Penn State/NCAR mesoscale weather model (MM5). Technical report, NCAR/TN-398+STR, National Center for Atmospheric Research, Boulder, Colorado, 1994.
[11] T. Gal-Chen, R.C.J. Sommerville, Numerical solutions of the Navier–Stokes equations with topography, J. Comput. Phys. 17 (1975) 276–310.
[12] A.E. Gill, Atmosphere-Ocean Dynamics, Academic Press, New York, 1982.
[13] F.X. Giraldo, J.S. Hesthaven, T. Warburton, Nodal high-order discontinuous Galerkin methods for the spherical shallow water equations, J. Comp. Phys 181 (2) (2002) 499–525.
[14] J.M. Greenberg, A.Y. Le Roux, A well-balanced scheme for the numerical processing of source terms in hyperbolic equations, SIAM Numer. Anal. 33 (1) (1996) 1–16.
[15] D. Hempel, Rekunstruktionsverfahren auf unstrukturierten Gittern zur numerischen Simulation von Erhaltungsprinzipien. PhD thesis, Universität Hamburg, Fachbereich Mathematik, 1999.
[16] J. Hunter, J. Keller, Weakly nonlinear high frequency waves, Commun. Pure Appl. Math. 36 (1983) 547–569.
[17] Z.I. Janjic, A nonhydrostatic model based on a new approach, Meteor. Atmos. Phys. 82 (2002) 271–285.
[18] P. Jenny, B. Müller, Rankine–Hugoniot–Riemann solver considering source terms and multidimensional effects, J. Comput. Phys. 145 (1998) 575–610.
[19] W.A. Gallus Jr., J.B. Klemp, Behavior of flow over step orography, Month. Wea. Rev. 128 (2000) 1153–1164.
[20] H. Kapitza, D.P. Eppel, The nonhydrostatic mesoscale model GESIMA. part I: Dynamical equations and tests, Beitr. Phys. Atmosph. 65 (2) (1992) 129–146.
[21] R. Klein, Asymptotic analyses for atmospheric flows and the construction of asymptotically adaptive numerical methods, ZAMM – Z. Angew. Math. Mech. 80 (2000) 765–777.
[22] J.B. Klemp, The weather research and forecasting (wrf) model. Technical report, National Center for Atmospheric Research, Boulder, Colorado, http://www-unix.mcs.anl.gov/~michalak/ecmwf98/final.html.
[23] J.B. Klemp, W.C. Skamarock, O. Fuhrer, Numerical consistency of metric terms in terrain-following coordinates, Month. Wea. Rev. 131 (2003) 1229–1239.
[24] B. van, Leer. Towards the ultimate conservative difference scheme. I. The quest of monotonicity, Lecture Notes Phys. 18 (1973) 163–168.
[25] B. van Leer, Towards the ultimate conservative difference scheme. II. Monotonicity and conservation combined in a second-order scheme, J. Comput. Phys. 14 (1974) 361–370.
[26] B. van Leer, Towards the ultimate conservative difference scheme. III. Upstream-centered finite-difference schemes for ideal compressible flow, J. Comput. Phys. 23 (1977) 263–275.
[27] B. van Leer, Towards the ultimate conservative difference scheme. IV. A new approach to numerical convection, J. Comput. Phys. 23 (1977) 276–299.

[28] B. van Leer, Towards the ultimate conservative difference scheme. V. A second-order sequel to Godunov's method, J. Comput. Phys. 32 (1979) 101–136.
[29] R.J. LeVeque, Numerical Methods for Conservation Laws, Birkhäuser, Basel, 1990.
[30] R.J. LeVeque, Balancing source terms and flux gradients in high-resolution Godunov methods, J. Comput. Phys. 146 (1998) 346–365.
[31] Ed. M.A. Alaka, The airflow over mountains. Technical report, WMO Tech. Note 34, 1960.
[32] A.J. Majda, R. Klein, Systematic multi-scale models for the tropics, J. Atmos. Sci. 60 (2003) 393–408.
[33] H. Nakamura, Dynamical effects of mountains on the general circulation of the atmosphere. I. Development of finite-difference schemes suitable for incorporating mountains, J. Meteor. Soc. Jpn. 56 (1978) 317–339.
[34] J. Pedlosky, Geophisical Fluid Dynamics, second ed., Springer, Berlin, 1987.
[35] J.-P. Pinty, R. Benoit, E. Richard, R. Laprise, Simple tests of a semi-implicit semi-Lagrangian model on 2D Mountain wave problems, Month. Wea. Rev. 123 (1995) 3042–3057.
[36] P. Queney, The problem of air flow over mountains: a summary of theoretical studies, Bull. Am. Meteor. Soc. 29 (1948) 16–26.
[37] R. Courant, K.O. Friedrichs, H. Lewy, Über die partiellen differenzengleichungen der physik, Math. Ann. 100 (1928) 32.
[38] K. Saito, The JMA NWP system and the Nonhydrostatic Model NHM. Technical report, Japan Meteorological Agency, Tokyo, ksaito@npd.kishou.go.jp.
[39] K. Saito, G. Doms, U. Schaettler, J. Steppeler, 3-D mountain waves by the Lokal–Modell of DWD and the MRI mesoscale nonhydrostatic model, Papers Meteorol. Geophys. 49 (1) (1998) 7–19.
[40] C. Schär, D. Leuenberger, O. Fuhrer, D. Lüthi, C. Girard, A new terrain-following vertical coordinate formulation for atmospheric prediction models, Month. Wea. Rev. 130 (2002) 2459–2480.
[41] C.W. Schulz-Rinne, The Riemann problem for two-dimensional gas dynamics and new limiters for high-order schemes. PhD thesis, Swiss Federal Institute of Technology, Diss. ETH No. 10297, 1993.
[42] A.J. Simmons, D.M. Burridge, An energy and angular-momentum conserving vertical finite-difference scheme and hybrid vertical coordinates, Month. Wea. Rev. 109 (1981) 758–766.
[43] R.B. Smith, Linear theory of stratified hydrostatic flow past an isolated mountain, Tellus 32 (1980) 348–364.
[44] P.K. Sweby, High resolution schemes using flux limiters for hyperbolic conservation laws, SIAM J. Numer. Anal. 21 (1984) 995–1011.
[45] J.P. Gerrit Jr., Z.I. Janjic, S. Nickovic, An alternative approach to nonhydrostatic modeling, Month. Wea. Rev. 129 (2000) 1164–1178.